01 Jan 2020

In-line Long Period Grating and Brillouin Scattering Fiber Optic Sensors for Strain, Temperature, Chloride Concentration, and Steel Mass Loss Measurement in Bridge Applications

Genda Chen
Missouri University of Science and Technology, gchen@mst.edu

Chuanrui Guo

FINAL REPORT

#INSPIRE-003

GRANT NO: 69A3551747126
GRANT PERIOD: 11/30/16 – 09/30/22
PROJECT PERIOD: 03/01/17 – 4/31/20

Inspecting and Preserving Infrastructure through Robotic Exploration (INSPIRE)

Tier 1 University Transportation Center Sponsored by the Office of the Assistant Secretary for Research and Technology (OST-R)

Project/Report Title:	**In-line Long Period Grating and Brillouin Scattering Fiber Optic Sensors for Strain, Temperature, Chloride Concentration, and Steel Mass Loss Measurement in Bridge Applications**
Consortium Member:	Missouri University of Science and Technology
Principal Investigator:	Genda Chen, Ph.D., P.E.
Co-Principal Investigator(s):	
Report Authors:	Genda Chen, and Chuanrui Guo

Missouri S&T · The City College of New York · Georgia Tech · CU · UNLV · N · East Central College · Lincoln · Ozarks Technical Community College · St. Louis Community College

DISCLAIMER

The contents of this report reflect the views of the authors, who are responsible for the facts and the accuracy of the information presented herein. This document is disseminated in the interest of information exchange. The report is funded, partially or entirely, by a grant from the U.S. Department of Transportation's University Transportation Centers Program. However, the U.S. Government assumes no liability for the contents or use thereof.

TECHNICAL REPORT DOCUMENTATION PAGE

1. Report No. INSPIRE-003	**2. Government Accession No.** (blank)	**3. Recipient's Catalog No.** (blank)
4. Title and Subtitle In-line Long Period Grating and Brillouin Scattering Fiber Optic Sensors for Strain, Temperature, Chloride Concentration, and Steel Mass Loss Measurement in Bridge Applications		**5. Report Date** 04/31/2020 **6. Performing Organization Code** CII
7. Author(s) Genda Chen, and Chuanrui Guo		**8. Performing Organization Report No.**
9. Performing Organization Name and Address Center for Intelligent Infrastructure (CII) Missouri University of Science and Technology 112 Engineering Research Laboratory, 500 W. 16th Street Rolla, MO 65409-0810		**10. Work Unit No.** (blank) **11. Contract or Grant No.** USDOT #69A3551747126
12. Sponsoring Agency Name and Address Office of the Assistant Secretary for Research and Technology U.S. Department of Transportation 1200 New Jersey Avenue, SE Washington, DC 20590		**13. Type of Report and Period Covered** Final Report Period: 03/01/2017 – 4/31/2020 **14. Sponsoring Agency Code** (blank)

15. Supplementary Notes

The investigation was conducted under the auspices of the INSPIRE University Transportation Center.

16. Abstract

This project developed an in-line grating and scattering fiber optic sensing system for strain, temperature, and steel mass loss measurement in bridge applications. Long period fiber gratings (LPFG) sensors are responsive to thermal and mechanical deformation, and the refractive index change of their surrounding medium. Brillouin scattering sensors are responsive to temperature and strain along an optical fiber. A CO_2 laser aided fiber grating system was assembled for LPFG fabrication. To enable mass loss measurement, a low pressure chemical vapor deposition (LPCVD) system was built to synthesize a graphene/silver nanowire composite film as flexible transparent electrode for the electroplating of a thin Fe-C layer on the curve surface of a LPFG sensor. Combined with two LPFG sensors in LP06 and LP07 modes for simultaneous strain and temperature measurement, three Fe-C coated LPFG sensors were multiplexed and deployed inside three coaxial steel tubes to measure critical mass losses through the penetration of tube walls and their corresponding corrosion rates in the life cycle of steel rebar. Thermal, loading and accelerated corrosion tests were conducted to validate the performance of the proposed sensors and demonstrate their feasibility for in-situ applications.

17. Key Words Corrosion sensor, long period gratings, graphene coating	**18. Distribution Statement** No restrictions. This document is available to the public.

19. Security Classification (of this report) Unclassified	**20. Security Classification (of this page)** Unclassified	**21. No of Pages** 68

Form DOT F 1700.7 (8-72) Reproduction of form and completed page is authorized.

EXECUTIVE SUMMARY

In this project, a LPFG based fiber optic sensor package was developed for simultaneous measurement of strain, temperature, and corrosion induced mass loss. Temperature and strain will induce changes in grating period and refractive index of LPFGs and thus cause resonant wavelength shift. For corrosion monitoring, a Fe-C layer was electroplated onto the graphene/silver nanowire (Gr/AgNW) coated LPFG due to its conductivity and optical transparency. The Fe-C layer has the same critical component ratio as steel rebar. The corrosion process changed the refractive index of the Fe-C layer and was calibrated with the resonant wavelength shift of the LPFG sensor through electrochemical impedance spectroscopy (EIS). Two different modes, LP06 and LP07, were fabricated for sensing in order to decouple strain and temperature. The performance of the LPFG sensor for corrosion monitoring was evaluated under various temperature and strain conditions. Modified correlation was established with different strain levels for more accurate mass loss estimation.

To protect the fragile fiber optic sensor and extend its service life, three miniature coaxial steel tubes with same thickness and length but different diameters were extracted from the steel rebar through electric discharge machining (EDM). An integrated fiber optic sensor package was fabricated alongside the fiber optic sensors. Thermal, loading, and accelerated corrosion tests were conducted on the proposed sensor package to validate its accuracy, robustness, and feasibility for in-situ applications.

ACKNOWLEDGMENT

Financial support for this INSPIRE UTC project was provided by the U.S. Department of Transportation, Office of the Assistant Secretary for Research and Technology (USDOT/OST-R) under Grant No. 69A3551747126 through INSPIRE University Transportation Center (http://inspire-utc.mst.edu) at Missouri University of Science and Technology. The views, opinions, findings and conclusions reflected in this publication are solely those of the authors and do not represent the official policy or position of the USDOT/OST-R, or any State or other entity.

Table of Contents

1 DESCRIPTION OF THE PROBLEM

Corrosion is a natural process that gradually destroys metal through an electrochemical reaction with its environment. The reaction gradually converts metal into a chemically stable form, such as oxide, hydroxide, and sulfide, which undermines its mechanical strength. In civil engineering, structures are often exposed to environments that accelerate the corrosion process of steel rebar: 1) deicing salt, seawater, and moisture to form electrolytes for electrochemical reactions; 2) chloride ion, CO_2, and sulfur contamination from the atmosphere to destroy the passivation film formed on the steel surface; and 3) tension stress/fatigue induced cracks that increase the contact area and penetration depth during the corrosion process. Corrosion induced deterioration of steel structures and steel bars in RC structures accounts for approximately $10B per year in direct costs and 10 times more in indirect costs in the U.S. Corrosion of steel reinforcement in RC structures is affected by a few factors such as age, surrounding moisture, chloride content, and permittivity of cover materials. Unless these factors are well understood using several corrosion detection tools, it is difficult to provide engineers with the definitive mass loss of steel elements required to evaluate the remaining capacity of steel members in practice.

Two main categories of corrosion monitoring techniques were developed based on measured parameters. Indirect methods usually focus on the measurement of corrosion related parameters. Their tests are easy to conduct but have compromised accuracy. As a rudimentary technique in the category of indirect methods, visual inspection has been used to monitor corrosion process. Images obtained from a camera include information such as corrosion dimensions, positions, and types. Different corrosion types are defined based on the appearance of the inspected area. Electrochemical techniques have been widely used in corrosion monitoring, especially in reinforced concrete (RC) structures. In most cases, electrochemical sensors are installed during the construction of RC structures. These sensors produce and

support the most used parameters in corrosion evaluation, such as open circuit potential, concrete resistivity, galvanic current, polarization resistance and moisture. The GPR technique is based on the propagation of an electromagnetic (EM) wave in concrete. An EM wave is first sent into the concrete structure and the reflected wave energy is then measured at the interface with two different dielectric constants. The propagation and reflection of the EM wave depends on the dielectric permittivity of the concrete, which is a function of temperature, moisture, chloride ion concentration, and corrosion level.

Commercial fiber optic sensors have been used to measure the corrosion-induced strain or the surrounding moisture that causes corrosion. For example, a chelating polymer coated LPFG sensor was developed to monitor moisture variations during the corrosion process under a simulated field environment, where the moisture measurements indicated how corrosive the environment was. Similarly, an azobenzene gel coated Fiber Bragg Grating (FBG) sensor was applied to measure corrosion-induced strains in steel rebar when confined in concrete. The FBG sensor was also applied directly around the steel rebar using super glue to measure the angular strain during the corrosion process as the volume of steel rebar expanded. An Extrinsic Fabry-Perot Interferometer (EFPI) was used to monitor the corrosion induced tensile strain in steel reinforced concrete beams. Correlations were established between the mass loss of steel rebar and the EFPI measured strain. For distributed fiber optic sensors, the Brillouin sensing technique was applied to measure the corrosion expansion of steel rebar in concrete by using a fiber optic foil winding method. The winding fiber optic measured the corrosion induced strain along the steel rebar surface through the Brillouin frequency shift. Compared to moisture measurements, strain measurements are more desirable for their stronger connection to corrosion products. However, an FBG sensor for strain measurements has a significantly decreasing sensitivity over time, which could be attributed to factors other than corrosion, such as the confinement of surrounding concrete and the interfacial properties. The EFPI sensor requires a highly accurate alignment between two fiber end surfaces to obtain robust fringe

visibility and can only measure one-directional strain. However, the strain distribution induced by corrosion in concrete is stochastic and the sensitivity of the signal decreases significantly over time. The Brillouin distributed fiber optic sensor can measure the strain distribution more precisely, but the correlation between the measured strain and the steel mass loss is indirect.

Direct approaches to assess the corrosion induced mass loss of steel were developed recently. In 2012, nano iron and silica particles were mixed with polyurethane and coated on the surface of a long period fiber gratings (LPFG) sensor by the PI's group to monitor the change in sensor resonant wavelength. However, the particle size, uniformity of coating thickness, coating transparency, and coating-fiber adhesive were less controllable. To improve these issues, a 0.8 µm thick inner layer of silver (for its conductivity) was deposited on the LPFG surface to electroplate a 20 µm thick outer layer of Fe-C materials (as a corrosion medium) on the sensor. Since the Fe-C layer has the same chemical component ratio as the steel rebar, the corrosion induced mass loss can be directly measured through the sensor's output. Although promising, its sensitivity and service life were limited by the low transparency and low silver-glass bonding factor of the silver layer, respectively. To mitigate these issues, a thin, conductive, and transparent film is required. In this project, the Gr/AgNW composite as a transparent and conductive film is applied to enhance the measurement performance (sensitivity and service life) of a Fe-C coated LPFG sensor for corrosion-induced mass loss in the Fe-C layer. Due to the high curvature of an optical fiber (125 µm in diameter), a random attachment of the Gr/AgNW composite to the curve surface of the LPFG poses a challenge since the intrinsic length of silver nanowires (100~200 µm) is in the same order as the diameter of the optical fiber, potentially causing air-entrapment and weak interfacial bonding. The solution proposed is to create a vacuum space between the Gr/AgNW film and the LPFG sensor so that they adhered to each other under external atmospheric pressure to provide the adhesion required during the electroplating process of the Fe-C layer.

For in-situ applications, long-term monitoring of corrosion usually takes years of operation. The proposed sensor can only provide mass loss measurement for approximately 60 hrs with zero strain, which is reduced to 30 hrs given a strain of 1500 με. Therefore, increasing the service life of the sensor is essential for long-term applications. Furthermore, the corrosion process is compounded by the strain induced by traffic and extreme loads, as well as daily and seasonal temperature changes. These factors can exist either simultaneously or separately. It is thus important to develop a new sensor package that can monitor these parameters at the same time. In this project, an integrated sensor is proposed, designed and tested for measurement of strain, temperature, and long-term corrosion induced mass loss in order to address the short service life. The sensor consists of three coaxial steel tubes in different diameters and five LPFG sensors. Two LPFG sensors in LP06 and LP07 modes, respectively, are utilized for strain and temperature sensing. Three Fe-C coated LPFG sensors are designed for corrosion induced mass loss measurement. The three steel tubes can not only protect the inside sensors from external mechanical forces and impact, but also provide three corrosion thresholds (in years) in practical applications. The use of the three steel tubes enables long–term monitoring of corrosion for assessing the life cycle of steel structures or steel reinforcing bars.

2 APPROACH

In order to monitor the corrosion induced mass loss, an Fe-C coated LPFG corrosion sensor was fabricated and calibrated in the SPAR Lab at Missouri S&T. The sensor fabrication processes included CO_2 laser grating, graphene synthesis and Fe-C electroplating. An integrated sensor package was also fabricated with three coaxial steel tubes, three Fe-C coated LPFG corrosion sensors, and two bare LPFG sensors in LP06 and LP07 modes for simultaneous strain, temperature and long-term corrosion induced mass loss measurement.

2.1 Ultrasensitive Fe-C coated LPFG corrosion sensor

An Fe-C coated LPFG corrosion sensor can monitor the corrosion induced mass loss with ultrahigh sensitivity with resonance wavelength shift. Fig. 2-1 illustrates the LPFG corrosion sensor. A bare fiber was firstly inscribed with long period grating through a CO_2 laser. Gr/AgNW was then transferred onto the LPFG surface for conductivity and transparency as the target layer. A 30-µm thick Fe-C film was then electroplated on top.

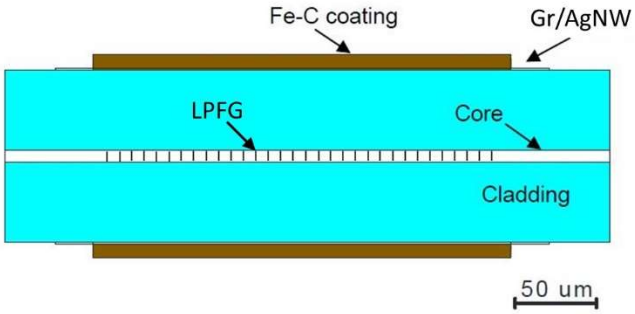

Fig. 2-1 Ultrasensitive Fe-C coated LPFG sensor for corrosion induced mass loss monitoring

According to electromagnetic and couple mode theory, the resonance wavelength λ_{res} of a LPFG can be determined by:

$$\lambda_{res} = (n_{eff}^{co} - n_{eff}^{cl,0j})\Lambda \tag{2.1}$$

where λ_{res} is the resonant wavelength of the sensor, and n_{eff}^{co} and $n_{eff}^{cl,0j}$ are the effective refractive index of the fiber core and j^{th} order cladding, respectively. Λ is the grating period.

As indicated in Equation (2.1), the resonant wavelength λ_{res} is proportional to both the grating period Λ and the difference in effective refractive index between the core n_{eff}^{co} and the j^{th} cladding mode $n_{eff}^{cl,0j}$. The effective refractive index of the cladding is determined by the indices of the core, the cladding and the surrounding medium. In comparison with Fiber Bragg Gratings (FBG) in sub-micron grating periods, which couples the forward propagating mode to the backward counterpropagating mode within the fiber core, LPFG sensors have the unique capability of monitoring changes in the ambient refractive index with extended applications in chemical, environmental, biological, and other related fields. The specially designed Fe-C coating has the same critical chemical component ratio with steel rebar in RC beams. The refractive index of the Fe-C changes with its corrosion process and thus can be correlated with the resonant wavelength shift of the LPFG sensor. The Gr/AgNW composite film is utilized for its conductivity and optical transparency in order to increase the sensor sensitivity.

2.2 Integrated sensor package for simultaneous strain temperature and corrosion induced mass loss measurement

An integrated sensor package was designed to protect the fragile fiber optic sensors and thus extend their service life while taking simultaneous measurements of strain, temperature, and corrosion induced mass loss.. Three tubes were extracted from a piece of steel rebar through electrical discharge machining (EDM). As shown in Fig. 2-2, the three tubes were arranged coaxially by placing smaller tubes inside larger ones. Three Fe-C coated LPFG corrosion sensors with yellow, green, and red fibers were placed inside each of the three tubes for corrosion-induced mass loss measurement. Two bare LPFG sensors in LP06 and LP07

modes, respectively, with blue and pink fibers as seen in Fig. 2-2 were deployed inside the inner tube for strain and temperature measurement. The two ends of the steel tubes were then sealed using marine epoxy.

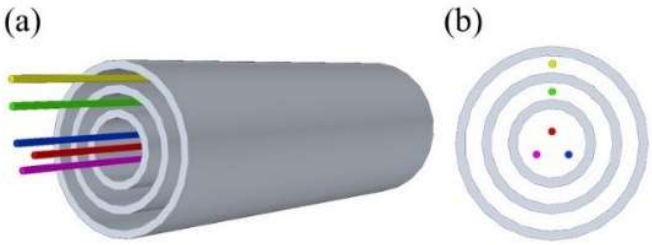

Fig. 2-2 Schematic view of an integrated sensor: (a) three-dimensional view and (b) cross section

3 METHODOLOGY

The designed sensors were fabricated and calibrated in order to investigate their performance in measuring temperature, strain, and corrosion induced mass loss.

3.1 Long period fiber grating sensor fabricated by CO_2 laser point-to-point inscription

The fabrication process used for the LPFG sensor is presented in this section. Section **Error! Reference source not found.** introduces the CO2 laser system used. Section **Error! Reference source not found.** calibrates the chloride ion concentration versus the resonant wavelength shift of the LPFG. Section **Error! Reference source not found.** presents the combined effects of the LPFG with Brillouin scattering. Section 3.1.4 investigates the maximum number of multiplexed LPFG sensors.

3.1.1 CO_2 laser aided optic fiber grating system

To fabricate a LPFG sensor, gratings were inscribed periodically in the core of an optical fiber. Inscription methods such as acid etching, acoustic wave and electric arc have been considered in the literature, but a CO_2 laser aided fiber grating system was instead developed for this project for higher speed and accuracy. The grating system mainly consists of a laser pulse inscription device and a high-resolution fiber movement mechanism. The laser output power and pulse duration are correlated to the refractive index modulation in the fiber core. Accuracy of the fiber movement determines the grating period and quality of the LPFG sensor.

Fig. 3-1 shows the CO_2 laser aided fiber grating system. It consists of a CO_2 laser source, a laser beam delivery system, a 3-axis manual linear stage, a single-axis motorized linear stage, controllers, a high-speed optical interrogator and a laptop computer. A laser source of 40 W was used to inscribe precisely the fiber with the output power tuned at 11.4 W with a 90-ms pulse duration.

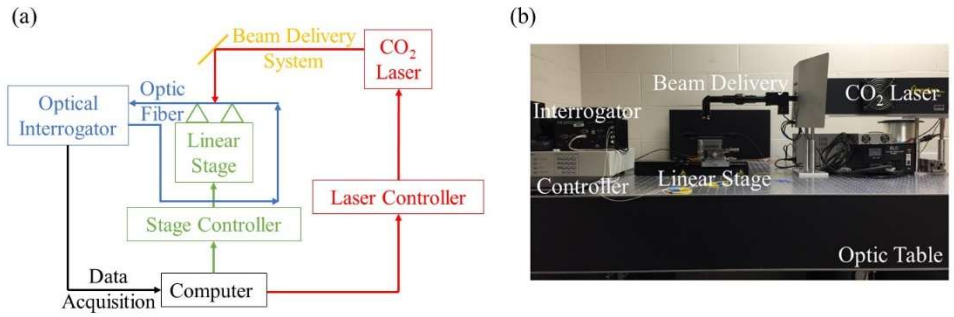

Fig. 3-1 The CO_2 laser grating system: (a) schematic illustration and (b) prototype

The beam delivery system contained a 3 times beam collimator and a ZnSe cylindrical lens to modulate the beam shape from a circle to a 90-µm wide and 200-µm long elliptical shape. The narrow elliptical shape of the laser beam improved the grating quality since it created a smaller heat affected zone. The 3-axis manual linear stage was used to adjust the distance between the fiber and the lens to meet the 25.4 mm focal length requirement. The single axis motorized linear stage controlled the horizontal movement of the fiber between two consecutive laser inscriptions so that various grating periods could be achieved. The laser and motorized stages were controlled by the customized MATLAB code compiled on each controller connected to the computer in order to adjust the laser pulse duration and grating period.

The grating procedure of a LPFG sensor can be summarized as follows:

a) Strip off 5 cm polymer coating on a SMF 28 optical fiber and clean it in a supersonic bath of isopropanol for 5 min.

b) Affix the cleaned fiber to the linear stage with two holders and connect the fiber to an optical interrogator.

c) Start the laser system and run the customized code in MATLAB to initiate the grating process. The MATLAB code controls the laser duration and grating period. The linear stage moves one step for

each grating period at a resolution of 0.1 µm.

d) Stop the laser and motorized stage once the attenuation of the LPFG transmission spectrum is 30 dB as illustrated in Fig. 3-2 for a typical LP06 mode. At a resonant wavelength of 1553 nm, the grating period for the LP06 mode is approximately 351 µm. To keep the same resonant wavelength (1553 nm), the grating period for the LP07 mode is approximately 303 µm.

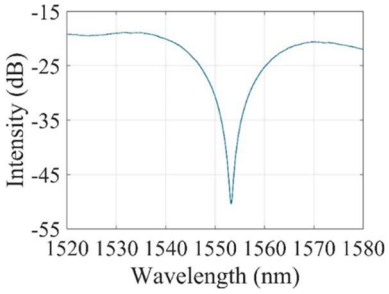

Fig. 3-2 Transmission spectrum of a CO_2 laser fabricated LPFG sensor

3.1.2 Calibration of chloride concentration measurement

Since the effective refractive index of the cladding $n_{eff}^{cl,0j}$ is partially determined by the refractive index of the surrounding medium, LPFGs have been widely used as a refractive index sensor to measure various parameters. For example, bare LPFG sensors were designed to measure pH, liquid level, and chloride ion concentration. Fig. 3-3 shows the wavelength shift of the LP07 LPFG sensor with a grating period of 303 µm with an increase of chloride concentration in a NaCl solution. For every 3.5% increase in chloride concentration by weight, the resonant wavelength shifts for approximately 1 nm.

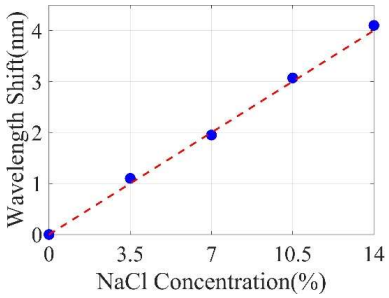

Fig. 3-3 Resonant wavelength shift of LP07 LPFG versus NaCl concentration

3.1.3 Combined sensing with LPFG and Brillouin scattering sensor

To investigate the interference effect between the LPFG sensor and the Brillouin optical time domain analysis (BOTDA), a bare LPFG sensor fabricated using laser power 11.4 W was fixed on the load frame to apply strain as shown in Fig. 3-4(a). Two ends of the fiber were connected to the optic interrogator (Micron Optics Si255) for LPFG transmission spectra acquisition. Fig. 3-4(b) shows the transmission spectra of the LPFG sensor under different strain levels. The BOTDA equipment (Neubrescope PPP-BOTDA) was the connected to the fiber loop for strain measurement. Fig. 3-4(c) compares the independent strain measurement results from the LPFG and the BOTDA, which indicated that there was no interference effect between the two types of sensors and thus could be combined together for in-situ applications.

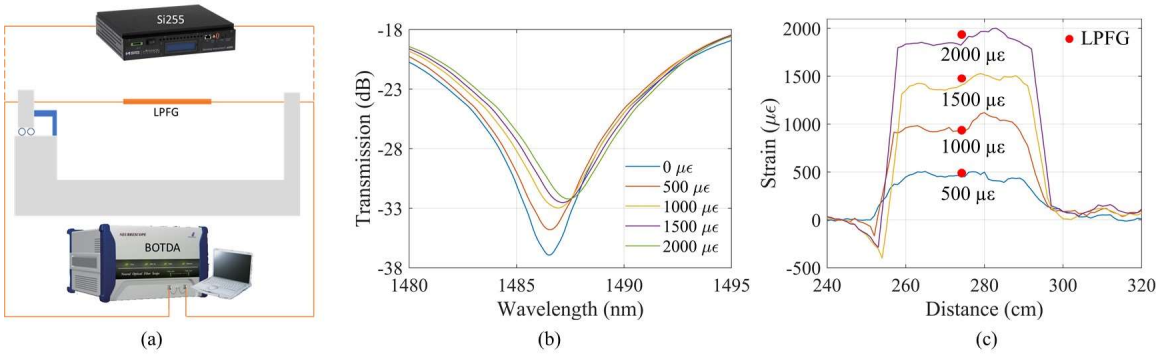

Fig. 3-4 (a) Test setup of BOTDA and LPFG combined strain sensing. (b) Transmission spectra of LPFG at different strain levels. (c) Comparison of strain measurement results

3.1.4 Maximum numbers of LPFG sensors for multiplexed sensing

To investigate the maximum number of LPFG sensors applicable for multiplex sensing, several LPFG sensors were fabricated through the laser grating system and then fusion spliced together. Considering the wavelength shift for strain, temperature, and corrosion induced mass loss monitoring, the recommended maximum number of LPFG sensors for one loop is six. The combined transmission

spectrum is shown in Fig. 3-5.

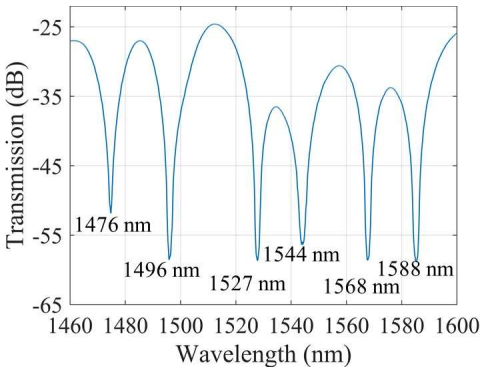

Fig. 3-5 Transmission spectrum of 6 multiplexed LPFG sensors

3.2 Low pressure chemical vapor deposition system for graphene synthesis

Graphene is a two-dimensional material that consists of a single layer of carbon atoms in a hexagonal lattice. It has attracted much attention since it was first produced from graphite in a lab through mechanical exfoliation. Due to its excellent optical, electrical, mechanical and thermal properties, graphene is an ideal material for transparent conductive films (TCF) in many applications, including flexible touchscreens, organic light emitting diodes (OLED), chemical sensors, soft robotics, actuators, and biological devices. In order to achieve industry-scale production, various graphene synthesis methods were developed by researchers, of which the chemical vapor deposition (CVD) technique is the most effective method due to its robust and large area monolayer graphene production. It is based on the chemical decomposition of carbon precursor gas under high temperatures and deposition of the carbon atom on a metal catalyst surface such as copper (Cu) or nickel (Ni).

3.2.1 LPCVD system in SPAR Lab MS&T for graphene synthesis

Figure 3-6 shows the LPCVD system used to grow graphene in this study. As shown in Fig. 3-6(a), the LPCVD system consisted of a few gas cylinders, a mass flow controller, a quartz tube chamber, a high temperature

furnace, a vacuum gauge, a pressure control valve, and a vacuum pump. CH_4 gas was used as the carbon source precursor, H_2 as the reduction gas, and Ar (Argon) as the protection gas. All the gases were pushed into the chamber by the mass flow controller with an accuracy of 0.1 sccm (standard cubic centimeter per minute). The quartz tube chamber was high-temperature resistant and heated to 1030 °C during the chemical reaction. The pressure control valve and the vacuum pump were designed to allow adjustments to the pressure level in the chamber. Figure 3.3(b) shows the laboratory prototype of the assembled LPCVD system.

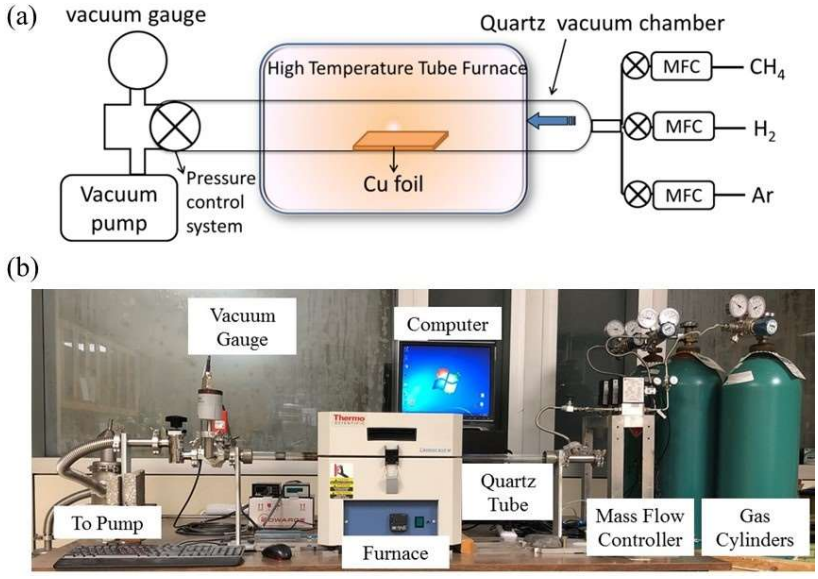

Figure 3-6 The LPCVD system: (a) schematic illustration and (b) laboratory prototype

The procedure used for graphene growth is summarized below:

1. Cut a copper foil (125 µm in thickness) into a 10cm×2cm square, clean it with a mixture of deionized water, acetone, and isopropanol in a wash bottle, and immerse the mixture into 99.9% acetic acid for 24 hrs. This step removes any oxides and organic contaminants on the copper's surface.
2. Place the cleaned copper foil into the quartz tube and move it to the center of the heat zone. Seal

the two ends of the quartz tube with metal collars and rubber O-rings.

3. Open the main valve and apply the vacuum. Check the pressure from the gauge reading to ensure that the vacuum has air pressure below 30 mTorr.
4. Allow 5 sccm H_2 and 5 sccm Ar into the chamber through the mass flow controller. The pressure should be kept under 100 mTorr.
5. Turn on the furnace to anneal the copper foil for 30 min. at 1030 °C.
6. Allow 5 sccm CH_4 into the vacuum for 10 min. As shown in Fig. 3-7, graphene flakes will start to grow gradually on the copper's surface and eventually expand into an integrated graphene layer. The darker lines indicate the grain boundary induced by the recrystallization of the copper under the high temperature.
7. Turn off the furnace and let the whole system cool down to room temperature. Turn off all the gases and close the vacuum pump.

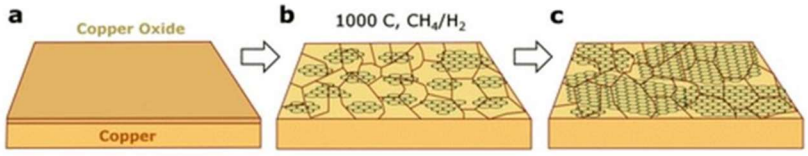

Fig. 3-7 Graphene growth process on the copper foil

3.2.2 Graphene/silver nanowire property calibration

Free standing samples of Gr/AgNW/Gr composites were fabricated using the vacuum annealing method in order to study their properties. As illustrated in Fig. 3-8, the vacuum annealing method is described below:

1. Spin coat a PMMA layer on the produced graphene on a copper foil at 4000 rpm for 30 sec.
2. Float the PMMA/Gr/Cu on copper etchant for 2 hrs in order to remove the remaining copper foil.

3. Wash the PMMA/Gr film in deionized water twice and flip it over to make the graphene layer on the top.
4. Transfer the Gr/PMMA film on the TEM grid and apply the AgNW on top.
5. Transfer another PMMA/Gr film on top of the sample.
6. Put the sample in the CVD chamber for 30 min. at 380 °C for vacuum annealing in order to evaporate the PMMA layer. After the annealing process, a suspended Gr/AgNW/Gr film is obtained on the TEM grid. A similar procedure can be followed to obtain free standing two-layer graphene without adding the AgNW.

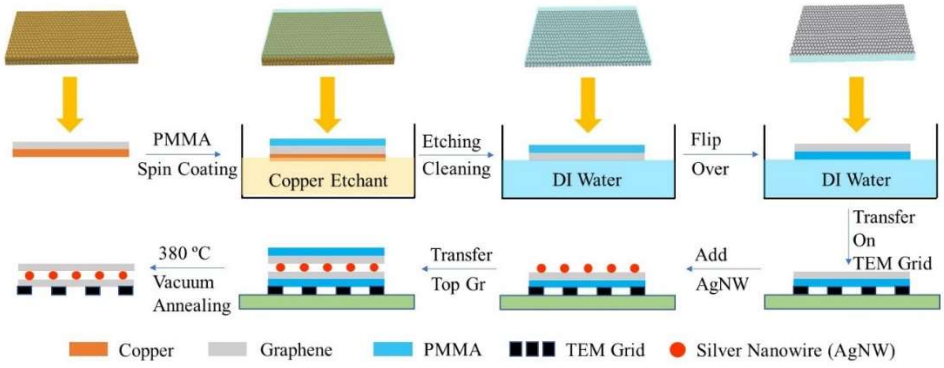

Fig. 3-8 Schematic procedure of the suspended Gr/AgNW/Gr composite synthesis

3.2.2.1 Silver nanowire average spacing

Fig. 3-9 shows the SEM images of the two-layer graphene and Gr/AgNW/Gr composites with different AgNW concentrations. Since the nanowires are irregularly distributed between two graphene layers, the average AgNW spacing is determined. Multiple measurements of the spacing were taken and averaged in order to obtain the average spacing value. As shown in Fig. 3-10, the average spacing decreases linearly from 4.2 µm to 1.5 µm with increasing AgNW concentrations.

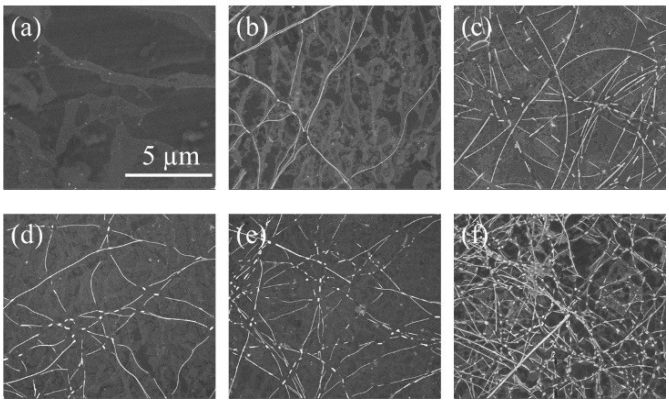

Fig. 3-9 SEM images of (a) two-layer graphene, (b)~(f) Gr/AgNW/Gr composite with an AgNW concentration of 0.2, 0.4, 0.6, 0.8, 1.0 mg/ml

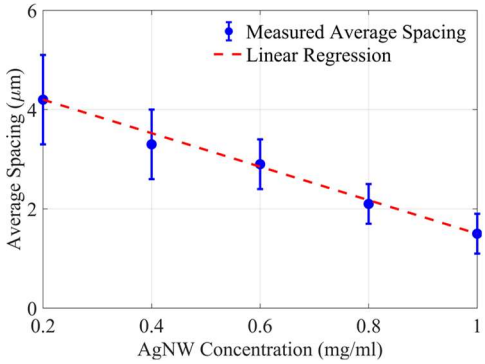

Fig. 3-10 AgNW average spacing with different concentrations

3.2.2.2 Optical transmittance

Fig. 3-11 shows a three-layer model of the thin film composite. It is introduced to characterize the optical transmittance of the composite. The wavelength of the light source is 550 nm, which is significantly larger than the AgNW's diameter (~30 nm). Therefore, the diffraction effect on the AgNW and interference between the two graphene layers are negligible. The total optical transmittance T can be expressed into:

$$T = \frac{I}{I_0} = T_G \cdot T_A \cdot T_G \tag{3.1}$$

where T_G and T_A are the transmittances of graphene layer and the AgNW network, respectively.

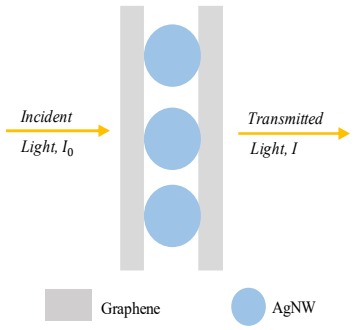

Fig. 3-11 A three-layer model of the thin film composite

The transmittance of graphene is T_G = 97% in monolayer and T_G = 93% in double layer. Table 3.1 lists the transmittances of the AgNW network, calculated and measured with five different AgNW concentrations. All the transmittances decrease with an increase in AgNW concentration. The proposed model fits the measured values well with a maximum error of 6%.

Table 3.1 Transmittance comparison of the calculated and measured value

AgNW Concentration (mg/ml)	AgNW Transmittance (measured)	Gr/AgNW/Gr Transmittance (calculated)	Gr/AgNW/Gr Transmittance (measured)	Error
0.2	87.7%	82.5%	85.7%	4%
0.4	86.6%	81.5%	80.6%	1%
0.6	85.0%	80.6%	79.1%	2%
0.8	83.5%	80.1%	77.6%	3%
1.0	79.3%	78.6%	73.7%	6%

3.2.2.3 Sheet resistance

The sheet resistance of the composite R_S is determined by three components: sheet resistance of the graphene layer R_G, sheet resistance of the AgNW network R_A, and contact resistance R_C between the graphene and the AgNW network. As shown in Fig. 3-12, three types of contact conditions between the AgNW network and graphene layer are defined based on their contact geometry. The sheet resistances of these three conditions (no contact, normal contact, and full contact) can be expressed by:

$$R_N = R_A \tag{3.2}$$

$$R_s = \frac{R_G^2(R_A + R_C) + R_C R_G(2R_A + R_C)}{2R_A(R_C + R_G) + (R_C + R_G)^2} \tag{3.3}$$

$$R_F = \frac{R_G + R_A}{2R_A + R_G} \tag{3.4}$$

The sheet resistance value R_G for monolayer graphene is about 275 Ω. The AgNW sheet resistance R_A was measured with different concentrations first. The sheet resistances of no contact and full contact conditions were then calculated using Equation (3.2) and (3.4). The sheet resistances of the composite were measured through the Four-Point method. The calculated and measured sheet resistances are compared in Fig. 3-13(a). It can be seen from Fig. 3.13(a) that the measured sheet resistance of the composite is between the upper and lower values calculated from the no contact and full contact models. Therefore, the normal contact model is appropriate for representing the average contact condition of the Gr/AgNW/Gr composite.

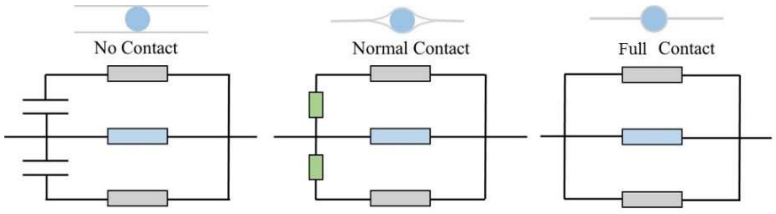

Fig. 3-12 Three circuit models of the composite sheet resistance

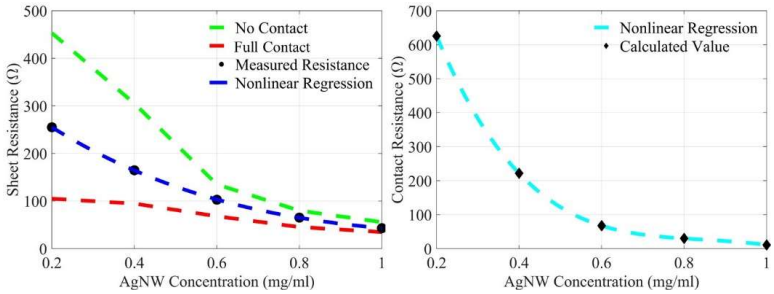

Fig. 3-13 Performance of three circuit models: (a) sheet resistances of no and full contact with the measured sheet resistance of the normal contact condition in between, and (b) calculated contact resistances with different AgNW concentrations

Based on the measured sheet resistances of the composite, contact resistances with different AgNW concentrations can be calculated from Equation (3.3) and are shown in Fig. 3-13(b). Nonlinear regression analysis was conducted for the sheet resistance R_S and the contact resistance R_C in order to establish their correlation to the AgNW concentration ϕ:

$$R_S = -137.5\phi^3 + 534.3\phi^2 - 735.6\phi + 382,\ R^2 = 0.98 \quad (3.5)$$

$$R_C = -2410\phi^3 + 5920\phi^2 - 4883.8\phi + 1384.2,\ R^2 = 0.96 \quad (3.6)$$

The measured sheet resistances of the AgNW network and the Gr/AgNW/Gr composite and the calculated contact resistance using the five different AgNW concentrations are listed in Table 3.2. All contact resistance values decrease with increasing AgNW concentrations similarly to the optical transmittances.

Table 3.2 Comparison of the calculated and measured sheet resistance

AgNW Concentration (mg/ml)	Measured AgNW Sheet Resistance Ω	Measured Gr/AgNW/Gr Sheet Resistance Ω	Calculated Contact Resistance Ω
0.2	453	255.1	625.5
0.4	305	164.7	221.7
0.6	135	102.9	67.6
0.8	79.9	65.3	30.1
1.0	55.8	43.1	10.9

3.2.2.4 Raman spectroscopy

Fig. 3-14 shows the Raman spectra analysis of the two-layer graphene and the Gr/AgNW/Gr composite. The Raman shifts at D, G, D', and 2D peaks and the intensity ratios of IG/I2D are listed in Table 3.3. The higher intensity at the D peak in the composite spectrum indicates the increasing disorder level of the sp^2 hybridization in the AgNW network between the two graphene layers. The localized vibration mode of AgNW also slightly splits the D' peak from the original G peak. The IG/I2D ratio is commonly used to determine the number of graphene layers. Since both samples have two layers of graphene, the ratios are close to each other.

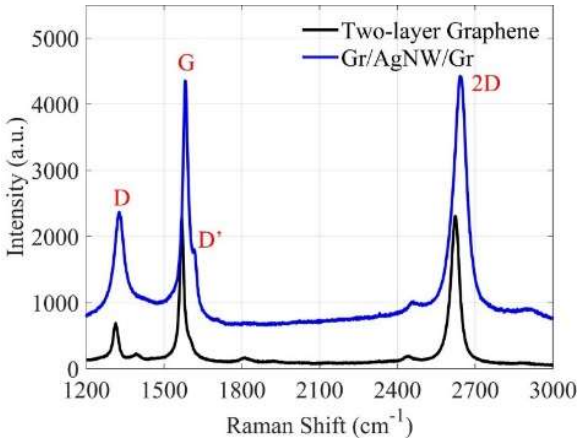

Fig. 3-14 Raman spectra of the two-layer graphene and the Gr/AgNW/Gr composite

Table 3.4 Intensity of each peak and ratio of G/2D

Sample	D-peak (cm^{-1})	G-peak (cm^{-1})	D'-peak (cm^{-1})	2D-peak (cm^{-1})	I_G/I_{2D}
Two-layer Gr	1319	1573	NA	2629	0.93
Gr/AgNW/Gr	1327	1582	1615	2642	0.98

3.3 Ultrasensitive LPFG corrosion sensor with graphene/silver nanowire based Fe-C electroplating

A transparent and conductive Gr/AgNW composite film is applied to enhance the measurement performance (sensitivity and service life) of a Fe-C coated LPFG sensor for corrosion-induced mass loss in the Fe-C layer. Section 3.3.1 introduces the sensor fabrication procedure. Section 3.3.2 characterizes the coating of the sensor. Section 3.3.3 investigates the calibration of the sensor under various strain and temperature conditions.

3.3.1 Sensor fabrication

One LPFG sensor with a Fe-C coating atop a Gr/AgNW/Gr film and a second coating atop a silver nano ink film were tested and compared. The Gr/AgNW/Gr-based sensor was prepared in three steps (LFPG, Gr growth, and Fe-C coating) while the silver ink was made similarly, whithout Gr growth.

Firstly, a bare LPFG was fabricated through the CO2 laser grating system introduced in Section 2. The

grating period of the fabricated LPFG sensors was 351 ± 0.1 μm with a total length of ~4 cm, revealing the LP06 cladding mode at 1520 nm wavelength.

Secondly, the LPFG sensor was coated with a Gr/AgNW/Gr conductive film according to the following steps as illustrated in Fig. 3-15:

a) A 25 mm × 100 mm copper foil with a thickness of 125 μm was placed in a chemical vapor deposition chamber and annealed at 1030 °C under 80 mTorr vacuum pressure with a 5 sccm hydrogen flow for 0.5 hrs. A 5 sccm methane flow was then added for 10 min. into the chamber to form a monolayer Gr on the copper foil surface.
b) The Gr (top) mounted copper foil was spin coated with a polymethylmethacrylate (PMMA) solution (20 mg/ml in chlorobenzene) at 4000 RPM for 30 sec. After 10 min heating under 180 °C to evaporate the chlorobenzene, a uniform PMMA film was applied on the Gr-copper surface.
c) The sample was immersed in copper etchant solution (Sigma Aldrich 667528) for 2 hrs in order to remove the copper substrate. The floating PMMA-coated Gr was then wet transferred into deionized water for removal of any copper residue.
d) The LPFG was fixed onto a microscope slide at two ends, placed into the deionized water underneath the PMMA/Gr film, and gradually lifted out of the water.
e) The two open ends allowed water between the LPFG and the PMMA/Gr film in order to create a vacuum space to firmly press the PMMA/Gr film against the curved surface of the LPFG under external atmospheric pressure.
f) The PMMA (m.p.=160 °C) was heated under 180 °C for 5 min in order to flatten any wrinkles before it was placed in an acetone bath for 20 min. A 0.4 mg/mL AgNW (ACS Material Inc.) solution in isopropyl was dropped onto the Gr-coated LPFG, spin coated at 100 RPM for 10 sec, and dried

at room temperature for 10 min to form a layer of the AgNW network. Repeat steps (a-e) to form the Gr/AgNW/Gr composite.

Thirdly, the Gr/AgNW/Gr composite was connected to the negative electrode in an electroplating solution (40 g/L $FeSO_4 \cdot 7H_2O$, 3.0 g/L L-ascorbic acid and 1.2 g/L citric acid) for 1.5 hrs with a current of 5 mA to form an approximately 30 µm thick Fe-C layer. To make a sound connection, the Gr/AgNW/Gr coated LPFG sensor was tightly fixed with marine epoxy at both ends onto a glass slide with minimum prestress to ensure that the sensor was horizontally straight. Silver nano ink (40w.t %, UT Dot. Inc.), a mixture of silver nano particles (approximately 10 nm) and xylene (b.p. =138.5 °C), was dip-coated onto the LPFG surface with a coating speed of 10 mm/s. This process was continued until the ink completely covered the connection area. After the ink was heated at 150 °C for 5 min to evaporate the xylene, a copper wire was placed on top of the ink and well covered with silver conductive epoxy, which then cured for 1 hr. Finally, the copper-Fe connection area was sealed with marine epoxy and cured for 24 hrs. Three sensors of each group were fabricated and tested based on the same procedure to ensure repeatability.

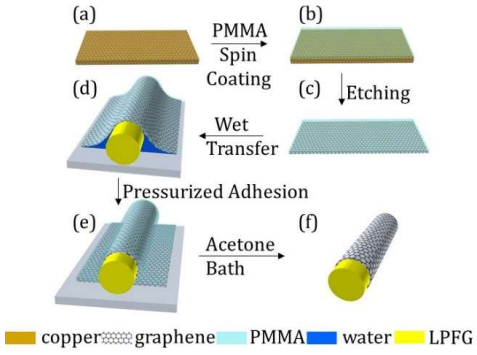

Fig. 3-15 Procedure of coating graphene on a LPFG sensor

3.3.2 Characterization of the coating

Fig. 3-16 shows the microstructure of the Gr/AgNW composite, cross section of the silver coated LPFG, thickness of the silver film, Fe-C grains, and the surface morphology of the Fe-C layer prior to corrosion

tests and after immersion in 3.5wt.% NaCl solution for 72 hrs under scanning electron microscopy (SEM, Helios Nanolab). The AgNW is approximately 30 nm in diameter and 100-150 µm in length. The Fe-C layer of approximately 30 µm thick has a dendritic structure with Fe-C grains approximately 27 nm in diameter. As shown in Fig. 3-16(b), the surface of the Fe-C layer is rough with a network of cracks, which is likely associated with remaining wrinkles in the Gr/AgNW film. The largest section measures approximately 500 nm in length. Fig. 3-16(c) and Fig. 3-16(d) show the cross section of the silver coated LPFG with a coating thickness of 170 ± 25 nm. After 72 hrs of immersion in the NaCl solution, the diameter of the Fe-C coated LPFG sensor became approximately 550 µm, including an approximately 215-µm thick layer of corrosion products that measures about 7 times the thickness of the original Fe-C layer.

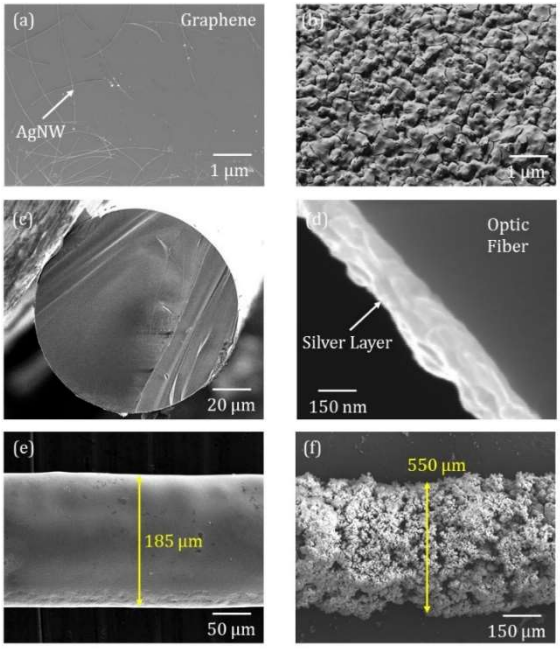

Fig. 3-16 SEM images of (a) Gr/AgNW/Gr composite, (b) Fe-C grains, (c) cross section of silver coated LPFG, (d) thickness of silver layer, (e) Fe-C coated LPFG before and (f) after 72 hrs of immersion in 3.5 wt. % NaCl solution

To ensure that three layers of Gr have been successfully coated onto the LPFG sensor, the Raman spectra of 1~3 Gr layers is firstly presented in Fig. 3-17(a). A G peak (1580 cm^{-1}) and a 2D peak (2680 cm^{-1}) are

clearly observed from each measurement. While the 2D peak is affected by the sp^2 bonding, the G peak varies with both the sp^2 bonding and the number of Gr layers. The intensity ratio (I_G/I_{2D}) between the G and 2D bands mainly represents the effect of the number of Gr layers. Specifically, the ratio increases with the number of Gr layers. The I_G/I_{2D} value of three-layer graphene is approximately 1.12. Raman spectra were then taken at different angles (Fig. 3-17(c)) on the Gr coated LPFG surface in order to investigate the angular homogeneity of the Gr distribution. Fig. 3-17(d) shows the I_G/I_{2D} value (1.12 ± 0.04) around the fiber surface, which indicates a robust Gr distribution. The D peak (1350 cm^{-1}) related to the disorder of the sp^2 bonding is not observed in Fig. 3-17(a), which indicates a uniform distribution of Gr on the local surface of the fiber at the measurement area.

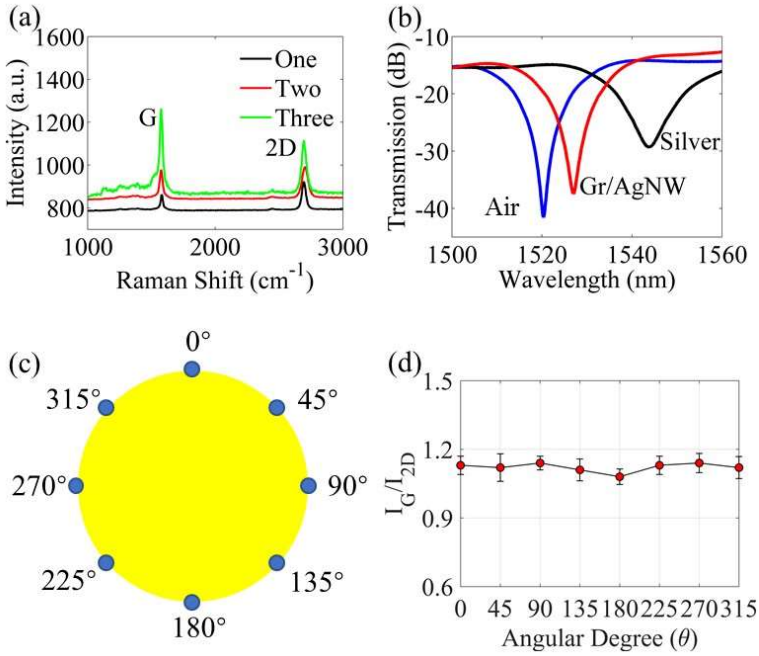

Fig. 3-17 Indication of Gr presence and its effect on the transmission of LPFG sensors: (a) Raman spectroscopy of 1~3 Gr layers, and (b) transmission spectra of bare, Gr/AgNW-coated and silver-coated LPFG. Raman spectroscopy taken at (c) different angular degrees around the LPFG surface and (d) IG/I2D values with variations reflecting the 3-layer graphene angular homogeneity on LPFG

3.3.3 Corrosion monitoring calibration

Correlation between the mass loss percentage of the Fe-C layer and resonant wavelength shift is calibrated through a 72-hour corrosion test combined with EIS and optical transmission spectra acquisition. The effects of various strain and temperature levels on sensor performance are also investigated.

3.3.3.1 Corrosion test under zero strain and room temperature in comparison with silver-based sensor

Two Fe-C coated LPFG sensors were calibrated for Fe-C mass loss measurement by simultaneously recording the resonant wavelength of each LPFG sensor and the corrosion rate of its Fe-C coating every 2 hrs, using a standard three-electrode setup for electrochemical impedance spectroscopy (EIS) tests. As shown in Fig. 3-18, the LPFG sensor was connected to a high-speed optical interrogator for transmission measurement. Simultaneously, the Fe-C coating and its substrate film (Gr/AgNW or silver nano ink), a platinum sheet, and a saturated calomel electrode were connected to a Gamry instrument (Potentiostat/EIS 300) to serve as a working, counter, and reference electrode, respectively. Prior to EIS tests, a stabilized open circuit potential (OCP) was recorded. The EIS measurements were then taken at 5 points per decade when a sinusoidal potential of 10 mV with a frequency range from 5 mHz to 100 kHz was applied around the OCP.

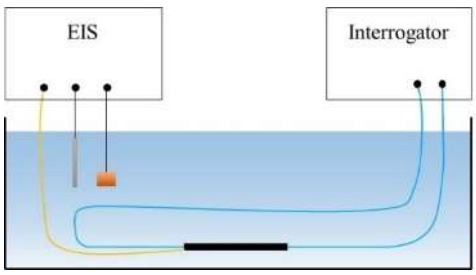

Fig. 3-18 Setup of the 72-hr corrosion test with EIS and optical spectra measurement

Fig. 3-19(a-1~a-3) and 3-19(b-1~b-3) show the transmission spectra of three Fe-C coated LPFG sensors based on the Gr/AgNW and silver films, respectively, over 72 hrs of immersion in 3.5 wt. % NaCl solution (1 spectrum every 2 hrs). The range of spectral shift of the Gr/AgNW-based sensor is significantly larger than that of the silver-based sensor. The blueshift of the transmission spectra of the Gr/AgNW-based sensor remains steady with increasing bandwidth over time.

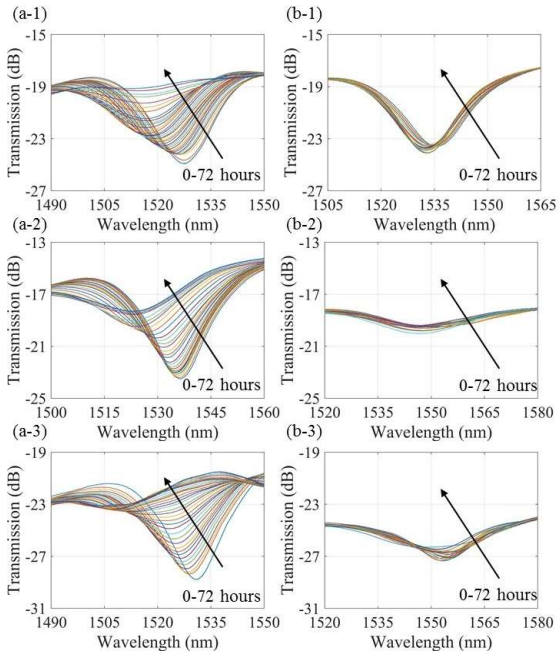

Fig. 3-19 Transmission spectra of the Fe-C coated LPFG sensors in 3.5 wt.% NaCl solution for 72 hrs: (a-1~a-3) Gr/AgNW-based film, (b-1~b-3) silver-based film

Fig. 3-20 shows the wavelength and transmission shifts of the Gr/AgNW- and silver-based LPFG sensors over time, respectively. For the silver-based sensor, the wavelength shift starts after about 10 hours of immersion and becomes saturated after 30 hours. For the Gr/AgNW-based sensor, the wavelength continues to decrease until approximately 46 hrs of immersion. That is, the service life (wavelength changing duration) of the Gr/AgNW-based sensor is 210% times that of the silver-based sensor. Fig. 3-20 also indicates that the transmission of the Gr/AgNW-based sensor increases steadily until 46 hrs of

immersion while that of the silver-based sensor remains nearly constant until 30 hrs and changes over time.

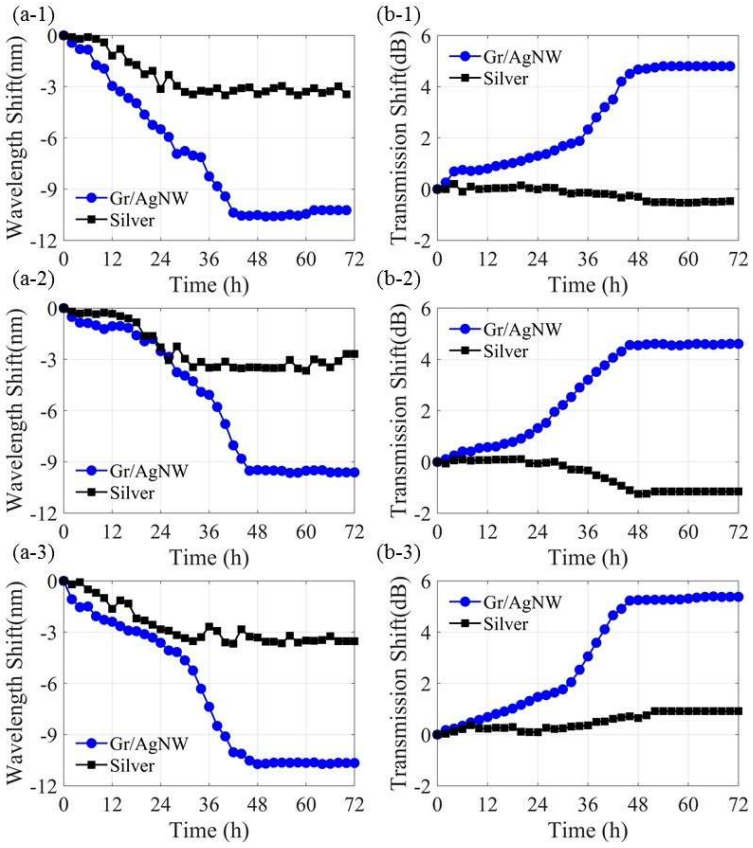

Fig. 3-20 Shift over time for the Fe-C coated LPFG sensors in 3.5 wt.% NaCl solution for 72 hrs: (a-1~a-3) wavelength and (b-1~b-3) transmission

Fig. 3-21(a-1) and Fig. 3-21(b-1) show the Nyquist plots (real Z_{real} versus imaginary Z_{img} components of a complex impedance) of the Fe-C coated LPFG sensors with Gr/AgNW- and silver-films, respectively. Each plot includes two semicircle arcs. The first small arc in high frequency range represents the combined properties of the Fe-C layer and the Gr/AgNW or silver film. The second large semicircle arc in low frequency range represents the electrochemical reaction at the Fe-electrolyte interface. The

electrochemical reaction can be represented by its charge transfer resistance (R_{ct}) and a double layer capacitance.

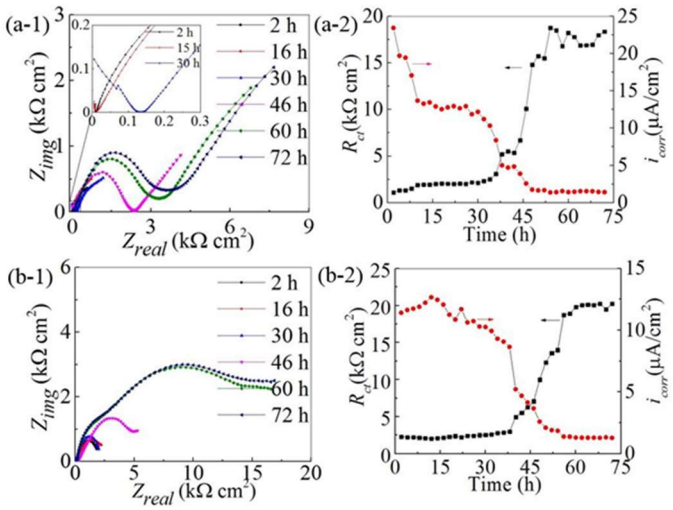

Fig. 3-21 Change of (1) Nyquist plots and (2) charge transfer resistance and corrosion current density of the Fe-C coating on (a) Gr/AgNW-based and (b) silver-based LPFG sensors in 3.5 wt. % NaCl solution up to 72 hours

Based on the Stern-Geary equation, the charge transfer resistance is inversely proportional to its corrosion current density, which can be related to the loss of Fe mass. Fig. 3-21(a-2) and 3-21(b-2) show the charge transfer resistance R_{ct} and its associated corrosion current density i_{corr} for the Gr/AgNW- and silver-based sensors, respectively. In general, when the charge transfer resistance increases over time, the corrosion current density decreases due to the continuing corrosion of the Fe-C layer. In particular, the corrosion current densities of the two sensors followed the same trend except in the first 10 hrs of corrosion tests, both indicating a near completion of the corrosion process of the Fe-C layers after 60 hrs. The exception was a very small resistance from the Gr/AgNW at the beginning of the tests, which may lead to notable errors in the conversion from resistance to corrosion current.

The corrosion current density was converted to the mass loss of the Fe-C layer using Faraday's Law. The mass loss was then divided by the initial mass of the Fe-C layer and presented in Fig. 3-22(a) with the silver

conductive film and Fig. 3-22(b) with the Gr/AgNW film. The normalized mass loss was 0% prior to corrosion and 100% after about 60 hrs of immersion in the NaCl solution. The normalized mass loss accumulated over time appeared independent of the type of conductive substrates used for the Fe-C electroplating.

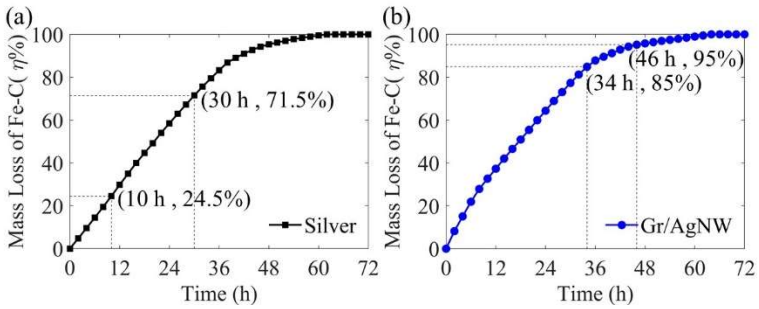

Fig. 3-22 Mass loss accumulated over time: (a) silver-based and (b) Gr/AgNW-based sensors

Finally, the wavelength and transmission shifts of the three samples presented in Fig. 3-20(a) and 3-20(b) were converted in Fig. 3-23(a) and 3-23(b) as a function of mass loss of the Fe-C layer. A LPFG wavelength shift of 10.3±0.3 nm was achieved with the use of the Gr/AgNW film and 3.4±0.1 nm with the silver film. Similarly, a LPFG transmission shift of 4.9±0.2 dB with the Gr/AgNW film and 0.8±0.1 dB with the silver film were achieved. Therefore, the use of the Gr/AgNW film significantly improved the sensitivity of the LPFG sensors.

As indicated in Fig. 3-23, the Gr/AgNW-based LPFG sensor with Fe-C coating responded to the corrosion process of the Fe-C coating in three stages: (I) gradual, (II) rapid and (III) stable. All linear regression lines correlated well with the test data. In Stage I, pitting corrosion started at locations on the surface of the Fe-C coating, and slowly progressed along the coating surface and inside the cracks until the NaCl solution fully penetrated the Fe-C coating after 34 hrs of immersion. This process gradually increased the effective refractive index of the Gr/AgNW-coated LPFG sensor and thus changed the resonant wavelength and transmission. In Stage II, once the NaCl solution was in contact with the generally impermeable Gr/AgNW

surface (0.36 nm in atom diameter), the pitting flakes on the remaining Fe-C coating spread both deeply and laterally until they were connected to cover a widening area of the Gr/AgNW surface after 46 hrs of immersion. In combination with a stronger evanescence field near the Gr/AgNW's surface, this corrosion process rapidly increased the effective refractive index and thus changed the wavelength and transmission 3.7 times as rapidly as those in Stage I. In Stage III, the effective refractive index of the surrounding environment basically remained unchanged, indicating that nearly the entire Fe-C layer had been corroded.

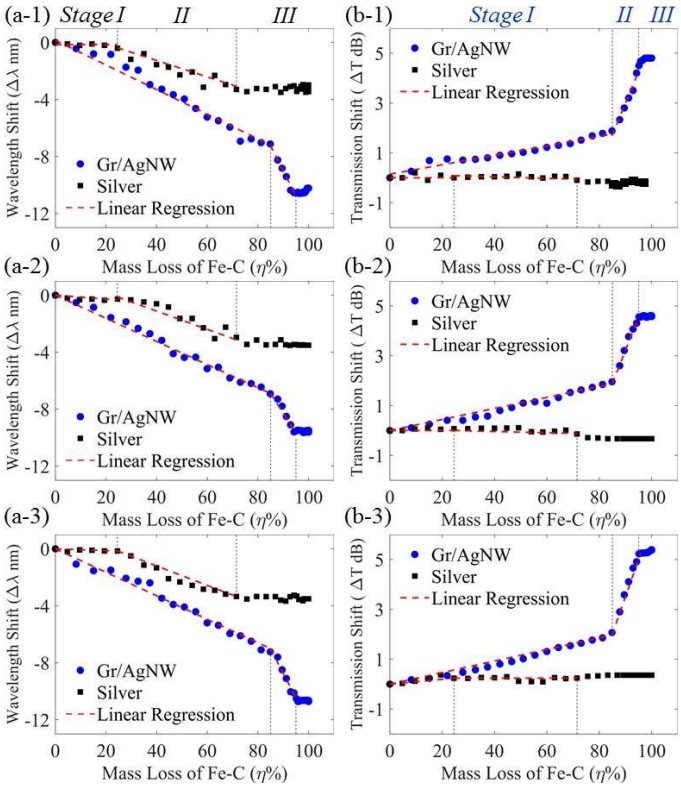

Fig. 3-23 Comparison of (a-1~a-3) wavelength and (b-1~b-3) transmission shift with Fe-C mass loss between the Gr/AgNW and silver films

3.3.3.2 Modified mass loss correlation under various strain levels

To investigate the corrosion monitoring performance of the proposed sensor at each strain level, a tensile test of Fe-C coated LPFG sensors was conducted in 3.5wt.%NaCl solution for 72 hrs with simultaneous EIS

and optical spectral measurements. Fig. 3-24 shows the schematic view and laboratory setup of a LPFG sensor on a loading machine.

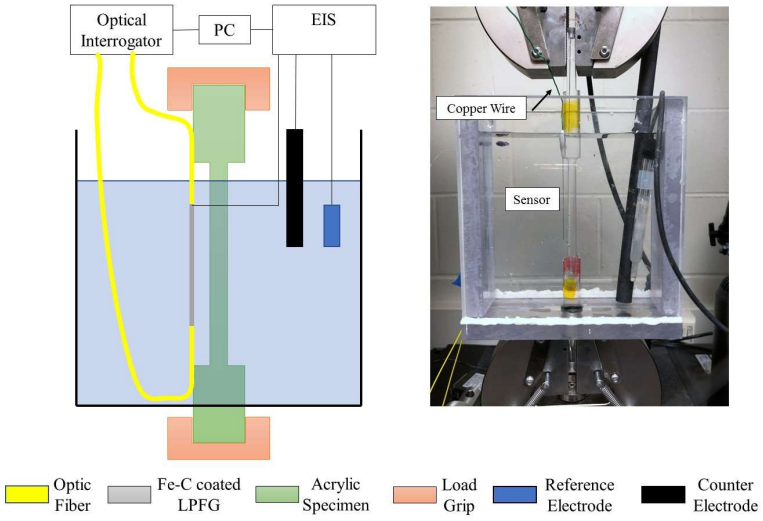

Fig. 3-24 Tensile testing of Fe-C coated sensors in 3.5wt.% NaCl solution: (a) schematic view and (b) laboratory test setup

As shown in Fig. 3-24, a Fe-C coated LPFG sensor was fixed on an acrylic dog-bone specimen and immersed in NaCl solution. The specimen was inserted into an open acrylic container through its bottom circular hole, which was sealed with a rubber O-ring to keep the NaCl solution in the container during testing. The top and bottom ends of the specimen were help in place by a low-capacity high resolution load frame (Instron 5965 with 5 kN max force and 0.001 N resolution). The optic fiber loop was connected to a 1 kHz optical interrogator in order to collect the transmission spectrum every two hours. For EIS tests, the Fe-C layer was connected to the Interface1000E Potentiostat/Galvanostat/ZRA (Gamry Instruments) equipment as the working electrode through a copper wire. The connection was covered with marine epoxy so as to avoid direct contact with the 3.5 wt.% NaCl solution. The solution was then poured into the container to fully immerse the sensor and three strain levels applied through the load frame. To make sure that the strain on the sensor was accurate, another bare LPFG was attached to the acrylic specimen

next to the Fe-C coated LPFG sensor in order to obtain the strain readout during testing and adjust the applied load accordingly. A total of nine Fe-C coated LPFG sensors were tested in this task, three of which were loaded to each of three strain levels for measurement repeatability.

The Fe-C coated LPFG was progressively subjected to three distinct strains (500, 1000 and 1500 με) and then fixed on an 18 mm diameter holder using 3000 psi glue for SEM imaging. Fig. 3-25 shows the SEM images of transverse cracks on the Fe-C layer at each of the three strains. It can be seen that the crack width increases from 7.9 to 24.9 μm as the strain increases from 500 to 1500 με. For statistical analysis, 10 measurements were taken to obtain the mean value and standard variation of crack widths.

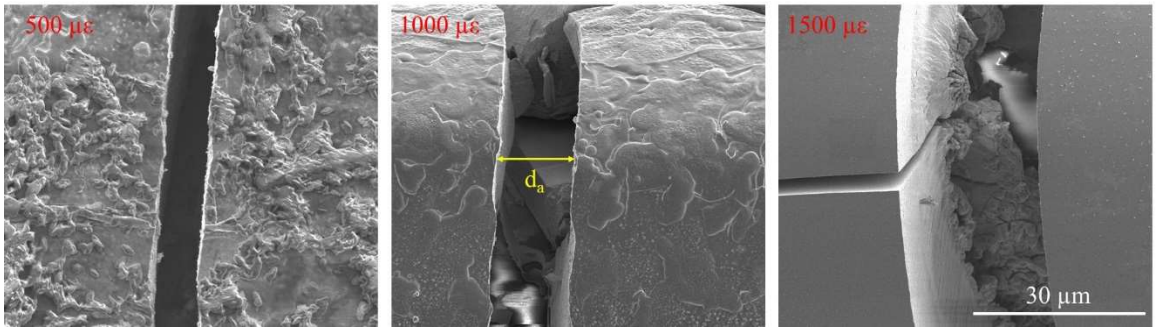

Fig. 3-25 Increasing width of transverse cracks on the Fe-C layer at three strains

The spacing of the transverse cracks is also an important parameter in crack distribution characterization. To show the crack spacing, SEM images were taken around every two adjacent cracks, scanning from one to another adjacent crack continuously. A full image covering two adjacent transverse cracks was then obtained by stitching together the continuous images. Up to 10 images were analyzed to obtain the average spacing. Fig. 3-26 shows the composite SEM images of two adjacent transverse cracks at each strain level. The spacing between the transverse cracks decreases with increasing strain, but the difference is insignificant in comparison with the change in crack width. Moreover, longitudinal cracks start to emerge at 1000 με and elongate at 1500 με. This result indicates that with increasing strain,

transverse fractures appear first and longitudinal fractures next due to the uneven distribution of the bonding strength between the fiber and Fe-C layers. The elongating longitudinal crack at increasing strain affects the corrosion process of the Fe-C layer more significantly since the NaCl solution can penetrate through the Fe-C layer more rapidly.

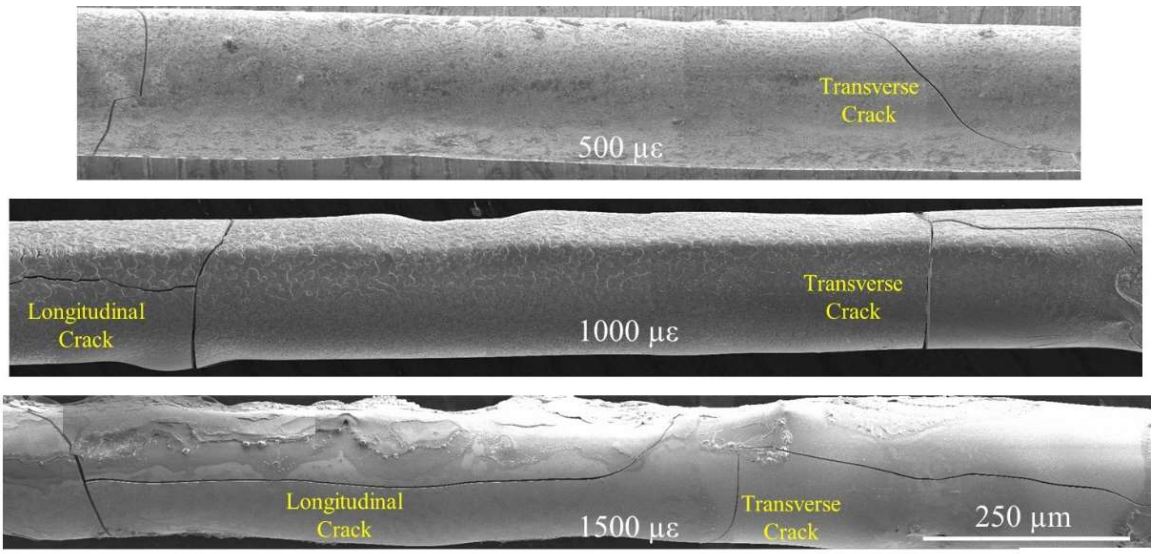

Fig. 3-26 Stitched SEM images along axial direction of the fiber showing two adjacent transverse cracks at each strain

Fig. 3-27 presents the transmission spectra of a representative Fe-C coated LPFG sensor tested for 72 hours at strain levels of 0, 500, 1000 and 1500 με, respectively. The shifts in resonant wavelength extracted from the spectra are plotted against time in Fig. 3-28. The increasing strain applied on the sensors causes wider transverse cracks and longer longitudinal cracks through which the NaCl solution can seep, thus accelerating the corrosion process of the Fe-C layer. It can be seen from Fig. 3-28 that the corrosion time for a complete loss of the Fe-C mass on each sensor is approximately 48, 42, 36, and 28 hrs at 0, 500, 1000 and 1500 με, respectively. However, the overall wavelength shift of every sensor remains approximately 10.4 nm, which is thus independent of the applied strain. The obvious three stages of corrosion in the bare Fe-C coated LPFG sensor, as observed in Fig. 3-28(a), gradually transitioned to two

stages of corrosion as the applied strain increased from 500, 1000, and 1500 με as shown in Fig. 3-28(b-d).

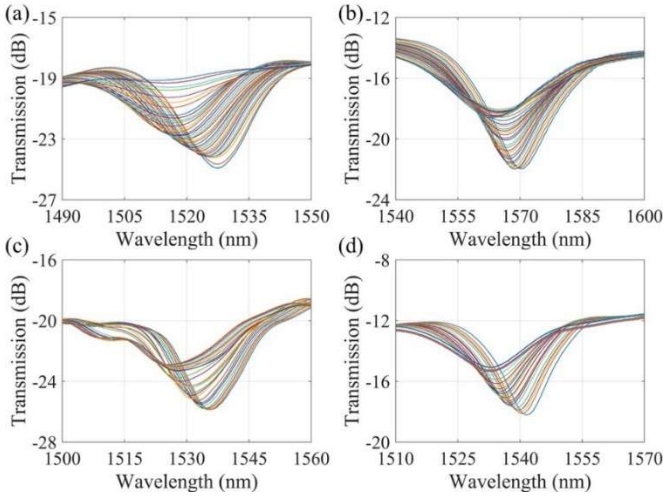

Fig. 3-27 Transmission spectra of the Fe-C coated LPFG sensors: (a) 0, (b) 500, (c) 1000 and (d) 1500 με for 72 hrs of corrosion test

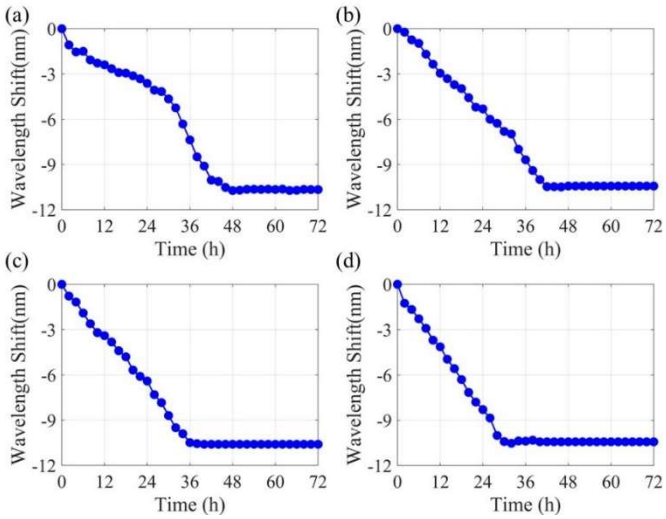

Fig. 3-28 Resonant wavelength shift over time: (a) 0, (b) 500, (c) 1000 and (d) 1500 με

Fig. 3-29 shows the Nyquist plots of four Fe-C coated LPFG sensors that were tested in 3.5 wt.% NaCl solution up to 72 hrs at 0, 500, 1000 and 1500 με, respectively. Due to the strain-induced cracks that penetrated through the Fe-C layer in each sensor, the electrolyte (NaCl solution) came in direct contact

with the Gr/AgNW film, significantly reducing the real and imaginary resistances. Therefore, the combined properties of the Fe-C layer and Gr/AgNW in the higher frequency range as shown in Fig. 3-29(b-d) are different from those in Fig. 3-29(a) for the zero-strain test.

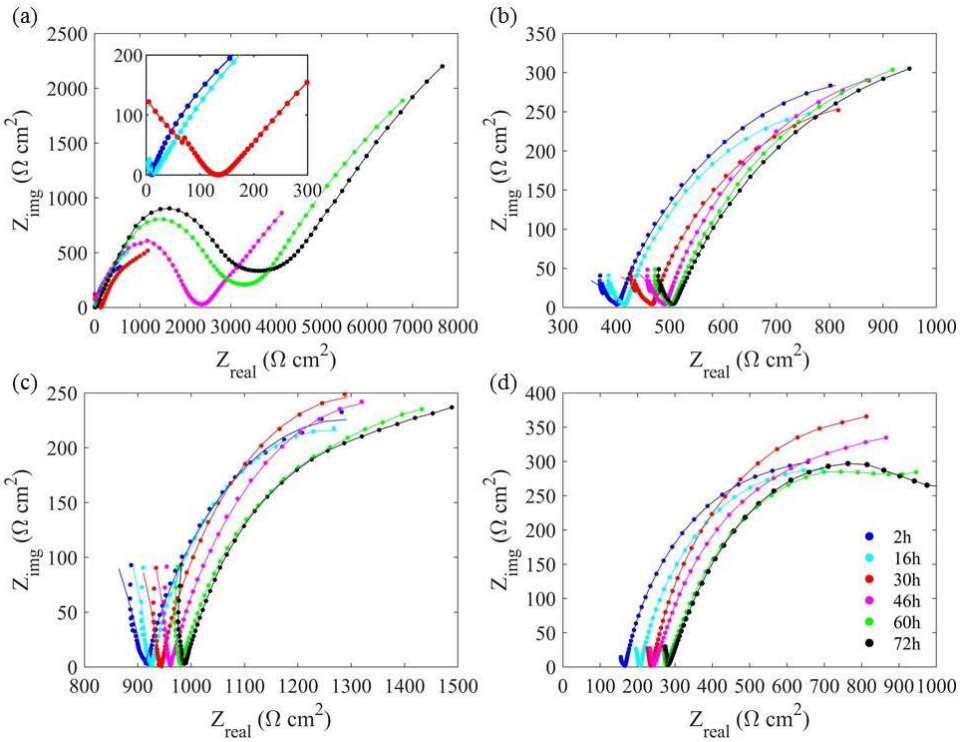

Fig. 3-29 Change of Nyquist plots of the Fe-C layer under (a) 0, (b) 500, (c) 1000 and (d) 1500 με in 3.5 wt. % NaCl solution up to 72 hrs

Fig. 3-30 shows the charge transfer resistance (R_{ct}) and corrosion current density (i_{corr}) of the Fe-C layer at each strain level. Corresponding to the wavelength shift over time as shown in Fig. 3-28, the charge transfer resistance increases over time in the three stages of corrosion at the zero strain, as shown in Fig. 3-30(a), and two stages of corrosion at a strain of 500, 1000 and 1500 με, as shown in Fig. 3-30(b-d). Based on the Stern-Geary equation, the charge transfer resistance is inversely proportional to the corrosion current density and can thus be related to the mass loss of the Fe-C layer as shown in Fig. 3-31.

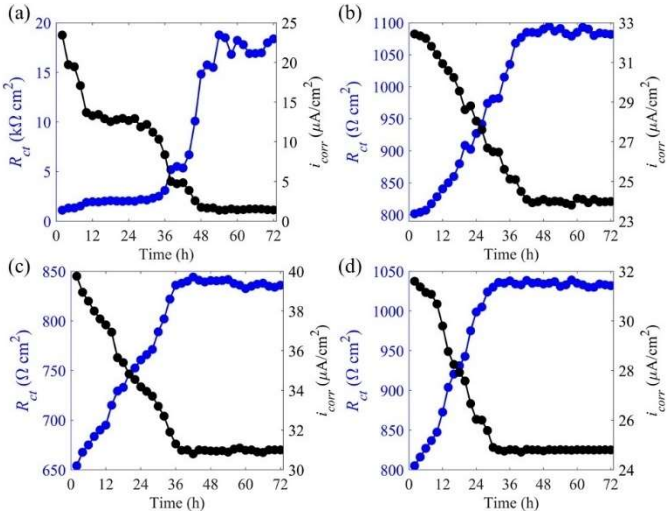

Fig. 3-30 Charge transfer resistance and corrosion current density of the Fe-C layers at (a) 0, (b) 500, (c) 1000 and (d) 1500 με

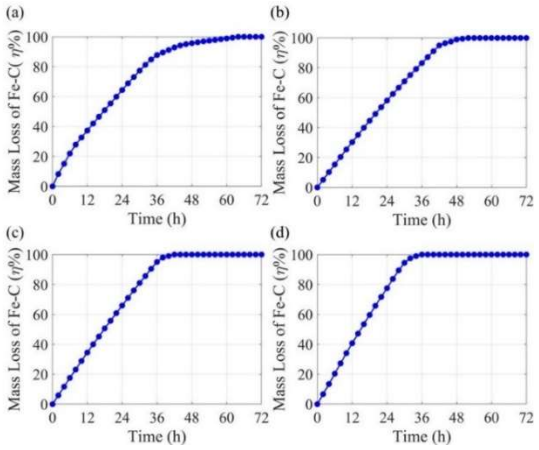

Fig. 3-31 Fe-C mass loss over time at (a) 0, (b) 500, (c) 1000 and (d) 1500 με

By combining Fig. 3-27 and 3-31, the resonant wavelength shift can be related to the mass loss of the Fe-C layer as presented in Fig. 3-32. In general, the entire corrosion process can be divided into three stages. Stage I represents the penetration process of the NaCl solution through the micro cracks and strain-induced cracks of the Fe-C layer (thickness), resulting in oxidization or uniform corrosion through the entire Fe-C layer. Stage II is associated with the continuing of the solution's penetration through the remaining Fe-C and, more importantly, the widespread reach of the solution at the Fe-C and Gr/AgNW interface, accelerating the uniform corrosion. Stage III is a stable stage wherein the Fe-C layer is

completely corroded away. Although they slightly increase the corrosion rate, the strain-induced cracks accelerate the penetration process of NaCl solution through the Fe-C layer in Stage I. Therefore, the total percentage of mass loss in Stage I decreases as the applied strain increases from 0 to 1500 με, thus resulting in the loss of more mass in Stage II.

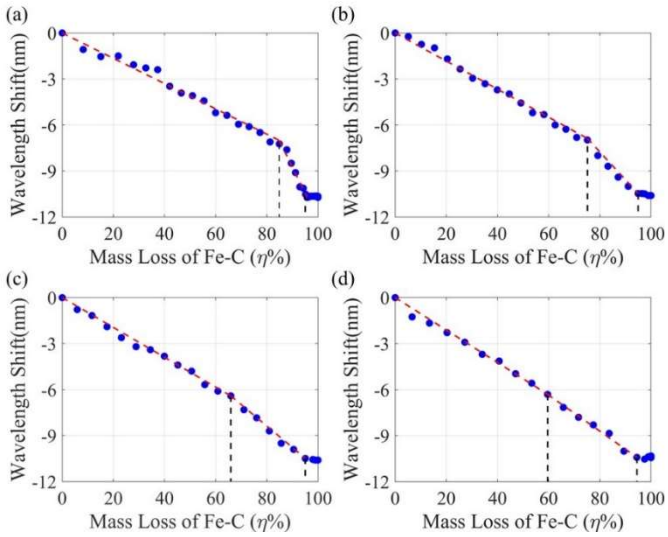

Fig. 3-32 Resonant wavelength shift with Fe-C mass loss at (a) 0, (b) 500, (c) 1000 and (d) 1500 με

The linear regression equation between the resonant wavelength shift and the Fe-C mass loss was derived at each strain level as presented in Fig. 3-32. The regression equations at different strain levels are listed in Equations (3.7) and (3.8) in Stages I and II, respectively. In all cases, the correlation coefficient exceeds 0.91, indicating a good fit of the linear regression lines into the test data in Fig. 3-32. The sensitivities of corrosion sensors at various strain levels are summarized in Table 3.5.

In stage I

$$\eta = (-10.99 \pm 0.2)\Delta\lambda, R^2 = 0.91 \quad 0\ \mu\varepsilon$$
$$\eta = (-10.31 \pm 0.3)\Delta\lambda, R^2 = 0.97 \quad 500\ \mu\varepsilon$$
$$\eta = (-9.52 \pm 0.1)\Delta\lambda, \quad R^2 = 0.95 \quad 1000\ \mu\varepsilon$$
$$\eta = (-8.93 \pm 0.1)\Delta\lambda, \quad R^2 = 0.94 \quad 1500\ \mu\varepsilon \qquad (3.7)$$

In Stage II,

$$\eta = (-2.89 \pm 0.4)\Delta\lambda + 62.25 \pm 4.1, R^2 = 0.93 \quad 0\ \mu\varepsilon$$
$$\eta = (-5.52 \pm 0.2)\Delta\lambda + 41.49 \pm 3.7, R^2 = 0.95 \quad 500\ \mu\varepsilon$$
$$\eta = (-7.14 \pm 0.3)\Delta\lambda + 22.93 \pm 1.8, R^2 = 0.92 \quad 1000\ \mu\varepsilon$$
$$\eta = (-8.47 \pm 0.4)\Delta\lambda + 4.96 \pm 0.5, \quad R^2 = 0.96 \quad 1500\ \mu\varepsilon \tag{3.8}$$

Table 3.5 Sensitivity of Fe-C coated corrosion sensors at various strain levels

Strain (με)	0	500	1000	1500
Sensitivity in Stage I (1% in mass loss/nm)	10.99	10.31	9.52	8.93
Sensitivity in Stage II (1% in mass loss/nm)	2.89	5.52	7.14	8.47

Fig. 3-33 presents the average wavelength sensitivities of three Fe-C coated LPFG sensors at each stage with one standard deviation of error correlated with the mass loss at the end of Stage I at various strain levels as illustrated in Fig. 3-31. In Stage I, since the strain-induced cracks allow more NaCl solution to penetrate through the Fe-C layer and increase the contact area of the Fe-C layer, the resonant wavelength shifts more rapidly and thus has a higher sensitivity to the mass loss than at zero strain. In Stage II, the bonding between the Fe-C layer and its underlying Gr/AgNW film is weakened, accelerating the electrochemical reaction of the Fe-C layer. Note that the change in refractive index of the NaCl solution during the corrosion process is negligible in both Stage I and II.

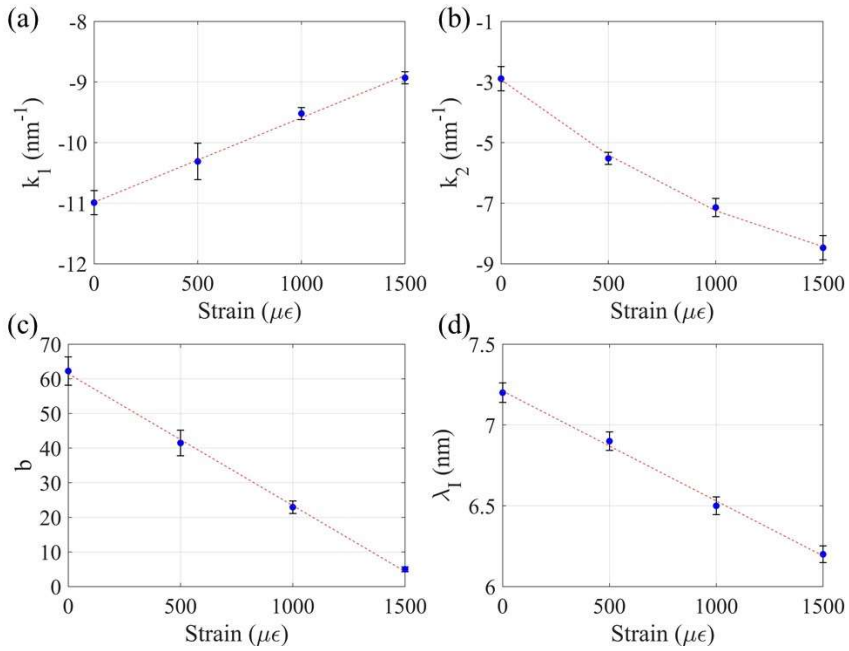

Fig. 3-33 Comparison and fitted curve of (a) Stage I sensitivity, (b) Stage II sensitivity and (c) mass loss at the end of Stage I at various strain levels

The average sensitivity increases linearly while in Stage I and decreases exponentially in Stage II with the increase in applied strain. The resonant wavelength shift can then be related to the mass loss at any strain level by:

$$\eta = k_1 \Delta\lambda \qquad \Delta\lambda \le \lambda_I \quad Stage\ I$$

$$\eta = k_2 \Delta\lambda + \mathrm{b} \qquad \Delta\lambda > \lambda_I \quad Stage\ II$$

$$k_1 = 0.0014\varepsilon - 10.99 \qquad R^2 = 0.93$$

$$k_2 = 1.3 \times 10^{-6}\varepsilon^2 - 0.0056\varepsilon - 3.93 \qquad R^2 = 0.95$$

$$b = -0.0381\varepsilon + 61.46 \qquad R^2 = 0.91$$

$$\lambda_I = -6.8 \times 10^{-4}\varepsilon + 7.21 \qquad R^2 = 0.96 \qquad (3.9)$$

in which the mass loss of the Fe-C layer can be calculated from the resonant wavelength shift that is extracted from the measured transmission spectra. This relation is referred to as the calibration equation.

To validate Equation (3.9), two strain levels, 700 and 1200 με, were considered in another set of corrosion tests on Fe-C coated LPFG sensors under tensile loading, using the same setup as illustrated in Fig. 3-24. Both the mass loss and the resonant wavelength of each Fe-C coated LPFG sensor were measured. Let η_m be the measured mass loss, η_{c1} be the mass loss calculated from zero stain condition, and η_{c2} be the mass loss calculated from Equation (3.9). The various mass losses corresponding to different wavelength shifts were obtained and compared in Table 3.6 with their respective measured values. It can be seen that, by using Equation (3.9) with the strain effect taken into account, the mass loss (η_{c2}) estimates are more accurate with a maximum error of 2.2% at 700 με and 2.5% at 1200 με. Both estimates are satisfactory in engineering applications.

Table 3.6 Comparison of the measured and calculated mass loss (%)

Δλ (nm)	η_{c1}	700 με				1200 με			
		η_m	Error	η_{c2}	Error	η_m	Error	η_{c2}	Error
2	27.1	19.9	36.2%	20.2	1.3%	18.5	46.5%	18.1	1.9%
4	49.1	39.5	24.3%	40.5	2.2%	37.2	32.0%	37.9	1.7%
6	71.0	59.8	18.7%	60.6	1.4%	55.2	28.6%	56.7	2.5%
8	93.1	80.1	16.2%	78.8	1.2%	73.4	26.8%	75.2	2.2%

3.3.3.3 Corrosion monitoring under various temperature conditions

To study the temperature effect on the process of corrosion monitoring, a temperature of 20, 40, and 60 °C was applied to the Fe-C coated LPFG sensor through the temperature-controlled water bath. As shown in Fig. 3-34, the Fe-C coated LPFG corrosion sensor was affixed onto the glass slide using marine epoxy. The fiber loop was then connected to a high-speed interrogator (Micron Optics Si255) for transmission spectra acquisition. The Fe-C layer was connected to a potentiostat (model: Gamry Interface 1000E) through a copper wire using silver conductive epoxy (MG Chemicals 8331) as the working electrode during electronic impedance spectroscope (EIS) tests. Open circuit potential (OCP) was measured before the EIS.

The EIS was conducted at 5 points per decade with a frequency range pf 5 mHz to 100 kHz and a sinusoidal potential of 10 mV around OCP.

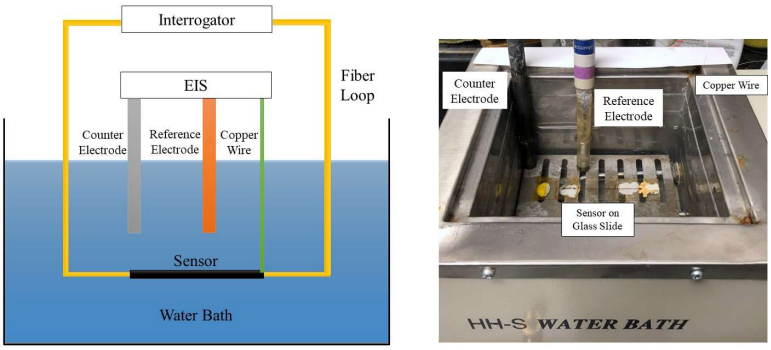

Fig. 3-34 Schematic view and laboratory setup of the corrosion test under various temperature levels.

The correlation between the mass loss of the Fe-C layer and the resonance wavelength shift was established using the method proposed and developed in our previous work. As shown in Fig. 3-35, the three stages as well as sensor sensitivity and transition mass loss between Stage I and II are considered to be the same for the three temperature conditions, indicating that the sensor has robust performance in pipeline corrosion monitoring under 60 °C.

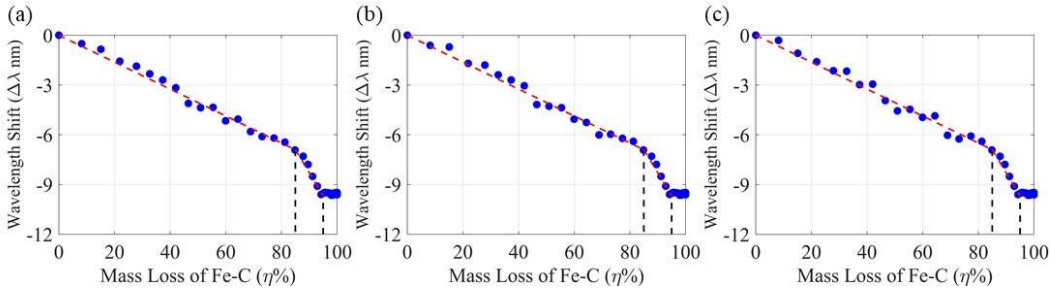

Fig. 3-35 Correlation between mass loss and resonance wavelength shift under three temperature levels.

3.4 Integrated sensor package for simultaneous strain, temperature and corrosion monitoring

Simultaneous multiparameter sensing of the integrated sensor package is described in this section. Section **Error! Reference source not found.** ~ 3.4.3 presents strain and temperature sensing results. Section 3.4.4 investigates the corrosion induced mass loss measurement.

3.4.1 Strain sensing

For strain calibration tests, a LPFG sensor was affixed onto the rebar with epoxy, which is then attached onto the load frame as illustrated in Fig. 3-36.

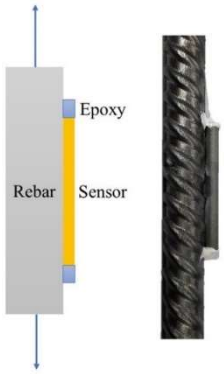

Fig. 3-36 Schematic illustration of the strain sensing setup

A total strain of 1000 με was applied to the rebar specimen with steps of 250 με. The transmission spectra of the LPFG sensor were recorded through the optical interrogator. The resonant wavelength shift with strain is shown in Fig. 3-37. The correlation between the resonant wavelength and strain is:

$$\Delta\lambda_{06} = 961.2\varepsilon, \quad R^2 = 0.97$$
$$\Delta\lambda_{07} = 1223.4\varepsilon, \quad R^2 = 0.98 \tag{3.10}$$

in which the LP_{07} mode is about 1.27 times more sensitive than the LP_{06} Mode. Since the LPFG sensor, in a steel tube, was attached to the rebar using epoxy, the strain transfer rate depends highly on the bonding strength between the two components in contact. If another bonding method is used, the correlation equation between the increasing strain and resonant wavelength shift must be recalibrated.

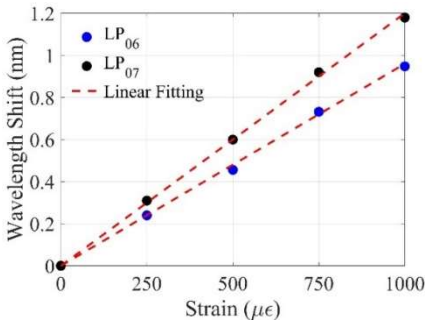

Fig. 3-37 Resonant wavelength shifts of LP06 and LP07 mode sensor with strain

3.4.2 Temperature sensing

For temperature calibration tests, a LPFG sensor was attached to a short piece of steel rebar with epoxy and immersed in the water bath as shown in Fig. 3-38.

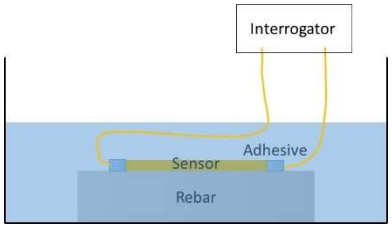

Fig. 3-38 Test setup for temperature calibration sensing

During the calibration tests, a temperature profile was taken, beginning from room temperature (25 °C) to 75 °C with an interval of 10 °C. The resonant wavelength shifts of the two LP modes were measured through a high speed optical interrogator (Micron Optics Si255). Figure 3-39 shows the wavelength shift with the increase in temperature of each sensor.

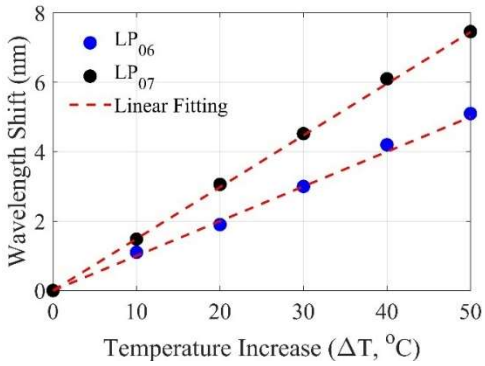

Fig. 3-39 Resonant wavelength shift of LP06 and LP07 sensors versus temperature increase

Therefore, the correlation between the temperature and resonant wavelength can be expressed into:

$$\Delta\lambda_{06} = 0.1\Delta T,\ R^2 = 0.95$$
$$\Delta\lambda_{07} = 0.15\Delta T, R^2 = 0.99 \quad (3.11)$$

The sensitivity of the LP_{07} mode is about 1.5 times higher than that of the LP_{06} mode. In concrete structures, the temperature around rebar will reach up to 70 °C during the concrete casting and hardening process due to hydration heat. Once this process is finished, the temperature will drop down to the environmental temperature. Therefore, a LPFG sensor can be used to monitor the change in early-age temperature in concrete. For steel structures, temperature changes usually come from the environment and extreme loads such as fire and explosions. In such cases, temperatures can rise to several hundred degrees Celsius. To monitor temperatures in such conditions, high-temperature resistant epoxy is required in order to provide reliable bonding of the sensor on its substrate. Equally important, if not more, is the fact that high temperature corrosion can also be monitored with the proposed sensor.

3.4.3 Simultaneous measurement of strain and temperature

The LP06 and LP07 LPFG sensors can be combined to discriminate the applied strain and temperature measurements due to their different sensitivity coefficients. To illustrate this point, the LP06 and LP07

sensors were deployed in a high temperature furnace with two ends attached to an external frame. As shown in Fig. 3-40, the left side of the frame is moveable controlled by a micrometer for strain application, while the right side of the frame is fixed.

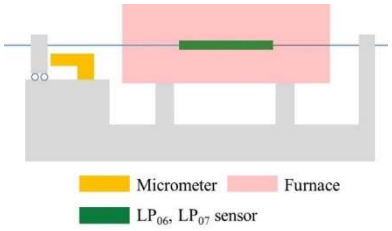

Fig. 3-40 Test setup for simultaneous strain and temperature measurement

During tests, the temperature in the furnace was increased from 50 °C to 200 °C at an interval of 50 °C. The strain applied on the LPFG sensor ranged from 0 to 4000 με with an interval of 1000 με. Both temperature and strain were applied simultaneously onto the sensors and their resonant wavelengths acquired from the optical interrogator. The measured strain and temperature were decoupled from the LP_{06} and LP_{07} mode wavelength shifts using the following equation:

$$\begin{Bmatrix} \Delta T \\ \varepsilon \end{Bmatrix} = \begin{Bmatrix} \alpha_{06} & k_{06} \\ \alpha_{07} & k_{07} \end{Bmatrix}^{-1} \begin{Bmatrix} \Delta\lambda_{06} \\ \Delta\lambda_{07} \end{Bmatrix} \tag{3.12}$$

where α is the temperature sensitivity and *k* is the strain sensitivity. As shown in Fig. 3-41 and Table 3.7, the decoupled strain and temperature from the sensor measurements match the load profile well with a maximum error of 4% in temperature and 8.2% in strain.

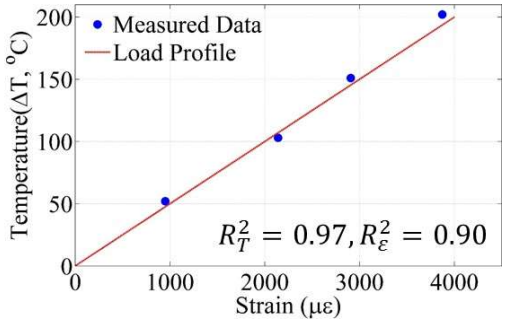

Fig. 3-41 Comparison of the measured data by LPFG sensor and the load profile

Table 3.7 Comparison of the applied and measured strain and temperature

Applied T (°C)	Measured T (°C)	Error	Applied Strain (με)	Measured Strain (με)	Error
50	52	4.0%	1000	962	3.8%
100	101	1.0%	2000	2164	8.2%
150	148	1.3%	3000	2869	4.4%
200	203	1.5%	4000	3750	6.3%

3.4.4 Long-term corrosion induced mass loss monitoring

In an integrated sensor composed of three steel tubes and three Fe-C coated LPFG sensors, each steel tube can delay the exposure time of a Fe-C coated LPFG sensor to keep it from reaching a specific pitting corrosion threshold for years or decades. As the NaCl solution reaches the LPFG sensor, the corrosion rate immediately after the corrosion threshold level can be measured. By combining the three tubes with the three Fe-C coated LPFG sensors, the integrated sensor can be used to measure three critical corrosion thresholds and their respective mass loss rates in the life span of steel structures. Since the natural corrosion process takes months or even years to complete, accelerated corrosion is used during laboratory tests by controlling the corrosion current density.

3.4.4.1 Mass loss calibration

The mass losses of steel tubes and rebar under various current densities were calibrated. Three combinations of a single tube A, a double tube A+B and a triple tube A+B+C were tested with the rebar. A bare LPFG was placed inside the inner tube of each combination in order to monitor the wall penetration time. The steel tubes were sealed with marine epoxy at each end and taped on the rebar. To investigate the effect of rebar length, three lengths (5 cm, 10 cm, and 15 cm) of rebar with a diameter of 16 mm were tested in three groups. Each rebar sample was then immersed in 3.5 w.t % NaCl solution for an accelerated corrosion test. To study the effect of the current density on mass loss, three current densities 500, 400, and 300 $\mu A/cm^2$, were applied to the rebar sample. The remaining mass of the tube and rebar were

measured daily. The resonant wavelength of the LPFG was also monitored daily. Once shifted, the resonant wavelength indicates that the steel tubes are fully penetrated. The test was then terminated. Fig. 3-42 shows the corroded rebar and steel tube penetration after the accelerated corrosion test.

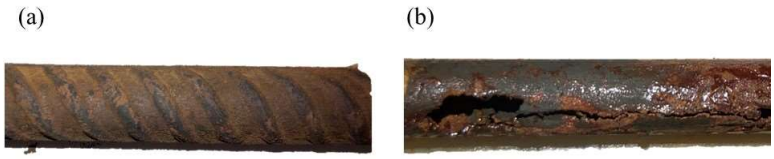

Fig. 3-42 Post-test examination: (a) corroded rebar and (b) corroded steel tube

Table 3.8 and Fig. 3-43 summarize the mass loss measurement results. The mass loss rates of the rebar and steel tubes increase with the current density but are not affected by the rebar length. This is because the increased rebar length required a larger current to keep the same current density; thus, the current density through the steel tube remained at the same level. However, with the double-layered and triple-layered tubes, the mass loss rate significantly decreases compared to the single-layered tube due to the increased total mass.

Table 3.8 Mass loss rate of the rebar and steel tube under different current densities

Sample	Current Density ($\mu A/cm^2$)	Rebar Mass Loss Per Day (%)			Steel Tube Mass Loss Per Day (%)		
		5 cm	10 cm	15 cm	5 cm	10 cm	15 cm
Single Tube	300	0.24	0.26	0.26	1.9	2.1	1.9
	400	0.33	0.35	0.32	2.6	2.7	2.5
	500	0.43	0.44	0.41	3.3	3.4	3.5
Double Tubes	300	0.21	0.22	0.27	1.2	1.3	1.1
	400	0.35	0.37	0.39	1.5	1.6	1.7
	500	0.46	0.42	0.47	2.1	2.0	2.2
Triple Tubes	300	0.21	0.25	0.28	1.0	0.9	1.0
	400	0.30	0.37	0.35	1.3	1.3	1.2
	500	0.41	0.46	0.47	1.6	1.5	1.6

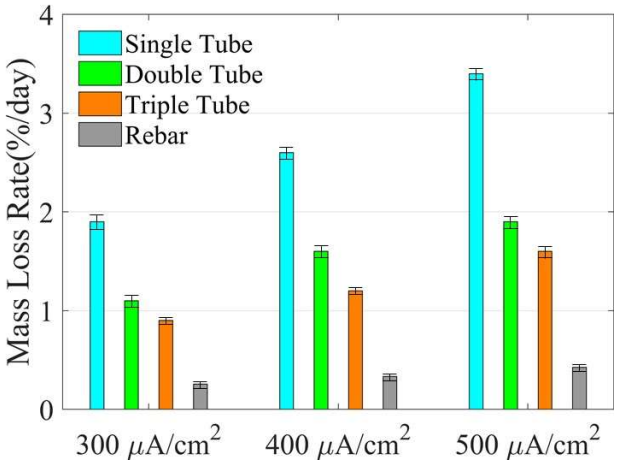

Fig. 3-43 Mass loss rates of the rebar and steel tube under various current densities

Fig. 3-44 shows the correlation of the mass loss rate between the rebar and steel tube. Despite the current density difference, the correlations follow a similar linear regression with different slopes. Let $\beta=d\eta/dt$ be mass loss rate, β_r be the mass loss rate of the rebar, β_1 be the mass loss rate of the single tube, β_2 be the mass loss rate of the double tube, and β_3 be the mass loss rate of the triple tube. Then the mass loss rate of the rebar can be represented by the mass loss rate of the steel tubes:

$$\beta_r = \frac{\beta_1}{7.91}, R^2 = 0.99$$

$$\beta_r = \frac{\beta_2}{4.84}, R^2 = 0.97$$

$$\beta_r = \frac{\beta_3}{3.73}, R^2 = 0.95 \quad (3.13)$$

Once the mass loss rate of the steel tube is obtained, the mass loss rate of the rebar can be derived using the above equations. Moreover, by multiplying the rate and time under a constant corrosion current density, the total mass loss of the rebar can be derived:

$$\eta_r = \beta_r \cdot t \quad (3.14)$$

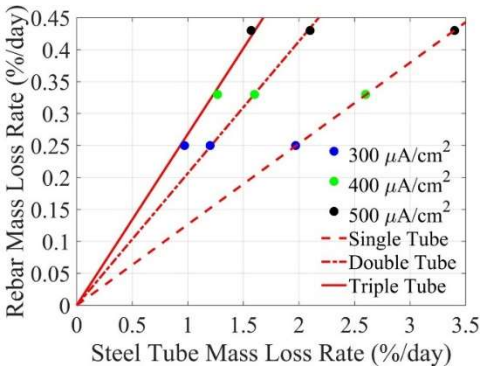

Fig. 3-44 Correlation of the mass loss rates between the rebar and steel tube

3.4.4.2 Penetration time of the steel tube

For long-term corrosion monitoring, it is important to understand how long it takes for the steel tube to be fully penetrated. This parameter determines the service life of the sensor and is critical for sensor design. Table 3.9 lists the penetration time of each tube combination monitored by the inner bare LPFG sensor under various current densities.

The penetration time through the wall of tube(s) decreased with the increasing current density due to the accelerated mass loss rate. A greater number of tubes needs a longer period to penetrate. Since the mass loss of the outer tube continued consuming current after it was penetrated locally, the total time it took to penetrate through the wall of the inner tube is not proportional to the number of tubes. The total mass loss of each tube and rebar after penetration was measured and compared in Table 3.10 with the value calculated by multiplying the penetration time and the mass loss rate.

Table 3.9 Penetration time of each tube combination under various current densities

Sample	Penetration Time (Days)		
	300 μA/cm^2	400 μA/cm^2	500 μA/cm^2
Single Tube	12	9	7
Double Tubes	27	21	16
Triple Tubes	46	35	28

Table 3.10 Total mass loss of rebar and steel tube after penetration

Sample	Current Density ($\mu A/cm^2$)	Steel Tube Measured Mass Loss (%)	Steel Tube Calculated Mass Loss (%)	Error	Rebar Measured Mass Loss (%)	Rebar Calculated Mass Loss (%)	Error
Single Tube	300	24.1	23.6	2.1%	3.2	3.0	6.3%
	400	24.5	23.4	4.5%	3.1	2.9	6.5%
	500	25.7	23.8	7.4%	2.8	3.0	7.1%
Double Tubes	300	35.1	32.4	7.7%	6.3	6.7	6.3%
	400	35.3	33.5	5.1%	6.5	7.0	7.7%
	500	32.4	33.6	3.7%	6.2	6.8	9.7%
Triple Tubes	300	46.5	44.5	4.3%	11.9	11.3	5.0%
	400	46.9	44.3	5.5%	12.4	11.7	5.6%
	500	42.1	43.9	4.3%	11.3	11.9	5.3%

3.4.4.3 Accelerated corrosion test of the integrated sensor with constant current density

Once the calibration of the mass loss and penetration time was finished, the long-term corrosion test for the integrated sensor could be conducted to validate its service life, accuracy, and reliability. As shown in Fig. 3-45(a), three Fe-C coated LPFG corrosion sensors (LPFGs 1,2 and 3) were deployed inside each steel tube, and both the sensors and tubes were sealed with marine epoxy at their two ends. Fig. 3-45(b) shows the assembled sensor prior to corrosion testing. The sensor was affixed onto a rebar measuring 16 mm in diameter and 20 cm in length with Kapton tape so that the mass loss of the rebar could still be measured daily by removing the sensor from the rebar. The entire sample was immersed into a 3.5 w.t % NaCl solution. The corrosion process of the entire sensor began from outside Tube A and continued until the stabilization of the inner LPFG 3. Two types of current density profiles were applied for the accelerated corrosion test. To simulate a stable corrosion environment, a constant current density of 500 $\mu A/cm^2$ was applied onto the sensor until the inner LPFG 3 was stabilized. To simulate the change of corrosion circumstances, the current density applied on the sample was set to 300 µA/cm2 before LPFG 1 was stabilized, then increased to 400 µA/cm2 before LPFG 2 was stabilizeds and finally increased to 500

μA/cm2 before LPFG 3 was stabilized. Transmission spectra of the LPFG sensors were recorded every two hours. Once the outer steel tube was penetrated, the inner Fe-C coated LPFG corrosion sensor started to monitor the mass loss rate at each critical stage.

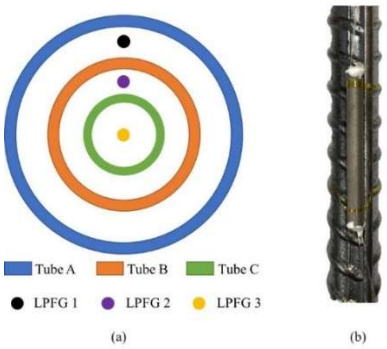

Fig. 3-45 Validation test setup of the integrated sensors: (a) schematic illustration of the sensor section and (b) assembled sensor on rebar prior to corrosion test

As shown in Fig. 3-46, the accumulated resonant wavelength shifts of the three LPFG sensors (1, 2, and 3) can be divided into three parts. Before the penetration of each tube, the inner LPFG sensor had no wavelength shift. After penetration, each LPFG sensor remained in working condition for about two days. The penetration times of the steel tubes are 7, 16, and 29 days, respectively.

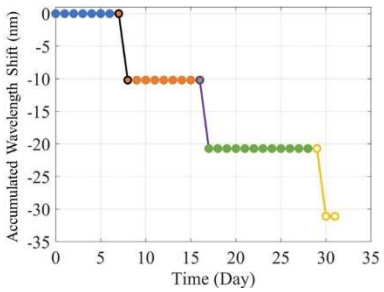

Fig. 3-46 Accumulated resonant wavelength shift over time under a constant current density

For the outer Tube A, the total mass loss at penetration is 24.8% from the calibration result. Since the current density is constant, the average mass loss rate can be calculated by dividing the total mass loss by the penetration time, resulting in a loss rate of 3.5% per day. The mass loss rate of the rebar can be

obtained using Equation (3.14). Thus, the total mass loss of the rebar can be estimated by multiplying its mass loss rate and penetration time. A similar procedure can be applied to the penetration of Tubes B and C by using the total mass loss of the double and the triple tubes from the calibration results. The estimated and measured mass loss of the rebar at each tube's penetration threshold are compared in Table 3.11. The estimation of the mass loss and rate is accurate within a maximum error of 8.8%.

Table 3.11 Comparison of the estimated and measured mass loss and rate of the rebar under a constant current density

Penetration of Tube	Estimated Mass Loss Rate (%/day)	Measured Mass Loss Rate (%/day)	Error	Estimated Mass Loss (%)	Measured Mass Loss (%)	Error
Tube A	0.44	0.48	8.3%	3.1	3.4	8.8%
Tube B	0.43	0.46	6.5%	6.9	7.4	6.8%
Tube C	0.42	0.46	8.7%	12.2	13.3	8.3%

The resonant wavelength shift over time for each LPFG corrosion sensor can be obtained from the transmission spectra as presented in Fig. 3-47. This relation is consistently observed to be nearly linear from all three LPFG sensors. The service life of the sensor was reduced to about 16 hrs due to the 500 $\mu A/cm^2$ current density. The mass loss of the Fe-C layer over time can thus be derived by using the correlation between the wavelength shift and the mass loss of the Fe-C layer. Since the total corrosion time of each sensor was 16 hrs, the average mass loss rate of each Fe-C layer equaled about 6.3% per hour.

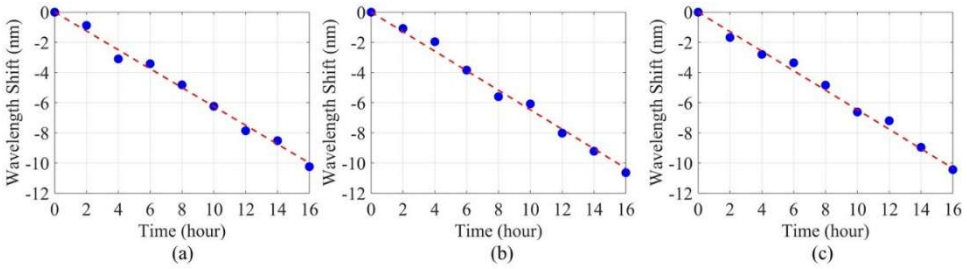

Fig. 3-47 Resonant wavelength shifts over time of (a) LPFG 1, (b) LPFG 2 and (c) LPFG 3 sensors under a constant current density (500 $\mu A/cm^2$)

3.4.4.4 Accelerated corrosion test of the integrated sensor with various current density

Fig. 3-48 shows the accumulated resonant wavelength shift of the three LPFG corrosion sensors over the entire lifecycle of the integrated sensor under a varying current density. The three tubes were penetrated at 12, 25 and 38 days, respectively. Since the current density is not constant, the mass loss rate cannot be obtained and used to estimate the rebar mass loss. However, the total mass loss of the rebar can still be estimated from the calibration results since the total mass loss of the rebar was not affected by the current density and remained at the same level at the time each tube was penetrated. As listed in Table 3.12, compared to the measured mass loss, the estimation is accurate within a maximum error of 9.1%.

As shown in Fig. 3-49, the resonant wavelength shift of each LPFG sensor can be obtained similarly to the constant current density test. Once again, the wavelength shift increases linearly with the test time before the Fe-C layer is completely corroded away. The service lives of the three sensors measured about 24, 20, and 18 hrs due to variation of the current density. The average mass loss rates of each Fe-C layer are listed in Table 3.13. The increased rate from LPFG 1 to LPFG 3 implies the increasing current density.

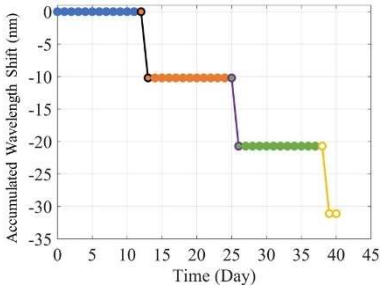

Fig. 3-48 Accumulated resonant wavelength shift over time under a varying current density

Table 3.12 Comparison of the estimated and measured mass loss of the rebar under a varying current density

Penetration of Tube	Estimated Rebar Mass Loss (%)	Measured Rebar Mass Loss (%)	Error
Tube A	3.0	3.3	9.1%
Tube B	6.3	6.8	7.4%
Tube C	11.9	11.2	6.3%

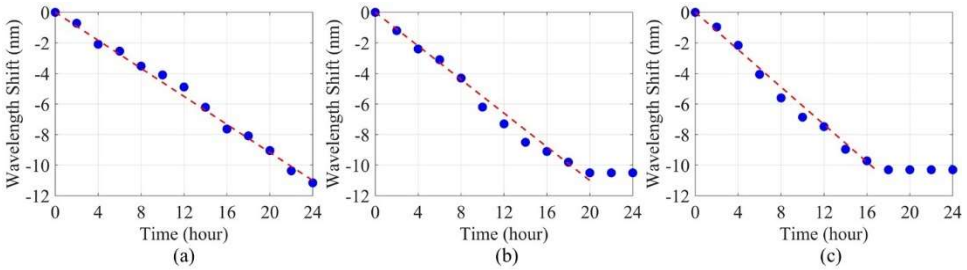

Fig. 3.49 Resonant wavelength shifts over time of (a) LPFG 1, (b) LPFG 2 and (c) LPFG 3 sensors under a varying current density

Table 3.13 Average mass loss rate of the Fe-C layer on each LPFG sensor

Sensor	LPFG 1	LPFG 2	LPFG 3
Mass Loss Rate (%/hr)	4.2	5.0	5.6

4 FINDINGS

In this project, an integrated fiber optic based sensor with laser aided manufacturing and nano material coating was studied systematically. First, a CO_2 laser grating system was designed and assembled for the fabrication of long period fiber gratings (LPFG). The wave and couple mode theory was introduced to explain the operational principle of the LPFG. In particular, two linear polarization (LP) modes, LP06 and LP07, were fabricated with different sensitivities for potential dual-parameter discrimination from one set of gratings in a single LPFG sensor. Then, to increase the sensitivity and service life of a Fe-C coated LPFG corrosion sensor, a thin composite film composed of graphene and silver nanowires was synthesized using a low pressure chemical vapor deposition (LPCVD) system that was specially designed and assembled as part of this study. The nano composite film was designed for the optimization of sensor efficiency and service life. An ultrasensitive corrosion sensor for mass loss measurement based on the Fe-C layer electroplated onto the Gr/AgNW coated LPFG was proposed, designed and tested. The calibration of the Fe-C coated LPFG sensor was also conducted under various strain levels for future in-situ applications. Finally, an integrated sensor composed of multiple LPFG sensors with their steel tube protection and extension were illustrated and validated for strain, temperature, and long-term corrosion monitoring in order to evaluate the critical corrosion thresholds of steel structures. Both constant and varied accelerated corrosion tests were conducted.

5 CONCLUSIONS

Based on the extensive experiments and data analyses performed, the following main conclusions can be drawn:

- The CO_2 laser grating system can fabricate both a LP06 mode LPFG sensor with a grating period of 351 µm and a LP07 mode LPFG sensor with a grating period of 301 µm in order to achieve a resonant wavelength of 1550 nm. The LPFG sensor can be used for strain, temperature, and refractive index sensing. Depending on the power of the laser source and the bandwidth of an interrogator, up to five LPFG sensors can be connected in series or multiplexed for multi-parameter measurements at discrete points using an optical spectrum analyzer (e.g., AQ6370C from Yokogawa).
- As-grown monolayer graphene can be synthesized on a copper foil using the LPCVD system. The graphene layer can be transferred while wet via a PMMA film onto a target substrate. It can be strengthened by silver nanowires for improved mechanical strength and electrical conductivity. The proposed vacuum annealing method proved effective for the synthesis of a suspended Gr/AgNW/Gr film on the TEM grid for property characterization. The optical transmittance and sheet resistance of the thin film decreased significantly and the stiffness of the film increased 4.6 times after the AgNW concentration exceeded 0.6 mg/mL. Based on these characterization test results, 0.4 mg/mL AgNW is recommended for sensor fabrication.
- The Gr/AgNW layer can be effectively adhered onto the curved surface of a LPFG sensor under atmospheric pressure on the vacuum space created around the sensor. A Fe-C layer can then be electroplated robustly onto the Gr/AgNW coated LPFG sensor for ultrasensitive corrosion induced mass loss sensing. Compared to the silver-based sensor, the Gr/AgNW-based sensor increased sensitivity by 1.9 times in Stage I and 7.2 times in Stage II due to its high optical transparency. The service life was also increased by 2.1 times.
- To investigate the effect of strain-induced cracks on the sensor performance, the Fe-C coated LPFG corrosion sensor was tested under three strain levels: 500, 1000, and 1500 µε. Transverse cracks appeared first and widened twice as the strain level increased from 500 to 1500 µε. However, the spacing between two adjacent transverse cracks decreased by less than 15%. At 1000 µε, longitudinal and inclined cracks began to emerge due to the uneven bonding (shear strength) between the Fe-C layer and the fiber's surface. They became significantly longer as the strain level increased from 1000 to 1500 µε. However, the width of the longitudinal and inclined cracks saw little change. In the corrosion monitoring tests, the strain-induced cracks on the Fe-C layer provided paths for the NaCl solution to seep into the surface of the LPFG sensor and thus caused the resonant wavelength to shift more rapidly. The calibration factor between the resonant wavelength and the Fe-C mass loss, which was established at zero strain, must be modified to take into account the effect of strain on the sensor. The modified calibration factor

was validated with a maximum error of 2.7% in mass loss estimation.

- The integrated sensor composed of three steel tubes and five LPFG sensors placed inside the tubes is rugged in field applications and effective for both long-term and short-term corrosion monitoring. Two LPFG sensors in LP06 and LP07 modes, deployed inside the inner steel tube, can be used for simultaneous strain and temperature compensation with high accuracy during short-term corrosion monitoring. The other three LPFG sensors coated with Fe-C can effectively measure the short-term corrosion rate of the Fe-C layer once in direct contact with the NaCl solution. The mass loss of the steel tubes is successfully correlated with that of a piece of steel rebar. For the double or triple tubes setup, the corrosion rate of the inner tube is lower than that of the single tube setup at the beginning of outer tube penetration. This is because both sides of the tube wall are connected to the electrolyte after penetration of the outer tube, thus consuming a relatively higher amount of the current. However, as the outer tube continues to corrode, it will eventually disconnect from the inner tube, gradually increasing its corrosion rate. Based on the accelerated corrosion test under a constant current density, the mass loss rate of a steel tube can be derived from its wall thickness and the time taken to fully penetrate the wall. The total mass loss and rate of the rebar near the steel tube can then be obtained from their correlation factor and the calibration factor between the Fe-C mass loss and the resonant wavelength shift. When the current density varies during the accelerated corrosion test, the mass loss rate of the steel tube cannot be acquired but the total mass loss of the rebar can still be estimated with high accuracy from the wall thickness of the steel tube. The Fe-C coated LPFG sensor provided the mass loss rate at each stage of corrosion.

6 RECOMMENDATIONS DEVELOPED AS A RESULT OF THIS PROJECT

In accordance with the current research, the recommendations for applying the integrated sensor package to strain, temperature, and corrosion sensing are listed as follows:

- The effect of strain on corrosion induced mass loss monitoring with the Fe-C coated LPFG sensor should be taken into consideration in measurements. Calibrations with various strain levels were conducted and modified correlations were established for a more accurate estimation of mass loss under different strain levels. Temperatures under 60 °C have negligible effect on the corrosion sensor's performance. However, further investigation is still needed to calibrate sensor performance if deployed to higher temperatures. The maximum number of LPFG sensors in one loop for multiplexed sensing should be six.
- The correlation of the mass loss rate between the steel tube and rebar needs further investigation into the natural corrosion process. A long-term in-situ test should provide helpful data, not only in the correlation between the steel tube and rebar, but also in understanding the relationship between the accelerated corrosion tests in the lab and the natural corrosion process on-site.

In summary, by utilizing the latest fiber optic, nano material and laser micromachining techniques, the research team has proposed and validated a novel LPFG based sensor package with demonstrated potential in the simultaneous measurement of strain, temperature, and corrosion induced mass loss. Fabricated with Gr/AgNW coating and Fe-C electroplating, the Fe-C coated LPFG corrosion sensor provides ultrahigh sensitivity and longer service life in comparison with the previous silver based sensor. Combined with the three coaxial steel tubes and dual LP mode LPFG sensors, the integrated sensor package can achieve long-term corrosion monitoring while monitoring the strain and temperature conditions at the same time. The proposed sensor package enables a robust and efficient solution for long-term structural

health monitoring in civil infrastructures.

7 REFERENCES

[1]. Panossian, Z.; de Almeida, N.L.; de Sousa, R.M.F.; de Souza Pimenta, G.; Marques, L.B.S. Corrosion of carbon steel pipes and tanks by concentrated sulfuric acid: a review. Corros. Sci. 2012, 58, 1–11.

[2]. Zaki, A.; Chai, H.K.; Aggelis, D.G.; Alver, N. Non-destructive evaluation for corrosion monitoring in concrete: A review and capability of acoustic emission technique. Sensors 2015, 15, 19069–19101.

[3]. Idris, S.A. Bin; Jafar, F.A.; Abdullah, N. Study on corrosion features analysis for visual inspection & monitoring system: An NDT technique. J. Teknol. 2015, 77, 59–65.

[4]. Bonnin-Pascual, F.; Ortiz, A. Corrosion Detection for Automated Visual Inspection. Dev. Corros. Prot. 2014.

[5]. Figueira, R. Electrochemical Sensors for Monitoring the Corrosion Conditions of Reinforced Concrete Structures: A Review. Appl. Sci. 2017, 7, 1157.

[6]. Deng, L.; Cai, C.S. Applications of fiber optic sensors in civil engineering. Struct. Eng. Mech. 2007, 25, 577–596.

[7]. Cooper, K.R.; Elster, J.; Jones, M.; Kelly, R.G. Optical fiber-based corrosion sensor systems for health monitoring of aging aircraft BT - Autotestcom 2001, August 20, 2001 - August 23, 2001. 2001, 847–856.

[8]. Moniruzzaman, M.; Rock, J. Azobenzene-Based Gel Coated Fibre Bragg Grating Sensor for Moisture Measurement. Int. J. Polym. Sci. 2016, 2016.

[9]. Casas, J.R.; Frangopol, D.M. Monitoring and reliability management of deteriorating concrete bridges. In Proceedings of the Proc., II International Workshop on Life-cycle Cost Analysis and Design of Civil Infrastructure Systems; 2001; pp. 127–141.

[10]. Maalej, M.; Ahmed, S.F.U.; Kuang, K.S.C.; Paramasivam, P. Fiber Optic Sensing for Monitoring Corrosion-Induced Damage. Struct. Heal. Monit. 2004, 3, 165–176.

[11]. Zhao, X.; Gong, P.; Qiao, G.; Lu, J.; Lv, X.; Ou, J. Brillouin corrosion expansion sensors for steel

reinforced concrete structures using a fiber optic coil winding method. Sensors 2011, 11, 10798–10819.

[12]. Huang, Y.; Gao, Z.; Chen, G.; Xiao, H. Long period fiber grating sensors coated with nano iron/silica particles for corrosion monitoring. Smart Mater. Struct. 2013, 22.

[13]. Chen, Y.; Tang, F.; Bao, Y.; Tang, Y.; Chen, G. A Fe-C coated long-period fiber grating sensor for corrosion-induced mass loss measurement. Opt. Lett. 2016, 41, 2306–2309.

[14]. Guo, C.; Fan, L.; Wu, C.; Chen, G.; Li, W. Ultrasensitive LPFG corrosion sensor with Fe-C coating electroplated on a Gr/AgNW film. Sensors Actuators, B Chem. 2019, 283, 334–342.

[15]. Tang, F.; Chen, Y.; Li, Z.; Tang, Y.; Chen, G. Application of Fe-C coated LPFG sensor for early stage corrosion monitoring of steel bar in RC structures. Constr. Build. Mater. 2018, 175, 14–25.

[16]. Chen, Y.; Tang, F.; Tang, Y.; O'Keefe, M.J.; Chen, G. Mechanism and sensitivity of Fe-C coated long period fiber grating sensors for steel corrosion monitoring of RC structures. Corros. Sci. 2017, 127, 70–81.

[17]. Fan, L.; Tang, F.; Reis, S.T.; Chen, G.; Koenigstein, M.L. Corrosion resistances of steel pipes internally coated with enamel. Corrosion 2017, 73, 1335–1345.

[18]. Fan, L.; Reis, S.T.; Chen, G.; Koenigstein, M.L. Corrosion resistance of pipeline steel with damaged enamel coating and cathodic protection. Coatings 2018, 8.

[19]. Fan, L.; Meng, W.; Teng, L.; Khayat, K.H. Effect of steel fibers with galvanized coatings on corrosion of steel bars embedded in UHPC. Compos. Part B Eng. 2019, 177, 107445.

[20]. Huang, Y., Chen, B., Chen, G., Xiao, H. and Khan, S.U. Simultaneous detection of liquid level and refractive index with a long-period fiber grating based sensor device. Meas. Sci. Technol. 2013, 24(9).

[21]. Guo, C.; Fan, L.; Chen, G. Corrosion-induced Mass Loss Measurement under Strain Conditions through Gr/AgNW-based, Fe-C Coated LPFG Sensors. Sensors. 2020, 20(6), 1598